

Fatigue Behavior of Direct Metal Laser Sintered (DMLS) Inconel 718

A thesis submitted by

Paul F. Kelley Jr.

in partial fulfillment of the requirements for the degree of

Master of Science

in

Mechanical Engineering

Tufts University

February 2016

Advisor:

Anil Saigal, PhD, Dept. of Mechanical Engineering, Tufts University

Committee Members:

Gary Leisk, PhD, Dept. of Mechanical Engineering, Tufts University

Anthony DiCarlo, PhD, The MITRE Corporation

[© 2015, Paul F. Kelley Jr.]

Abstract

In the rapidly growing field of additive manufacturing (AM), the focus in recent years has shifted from prototyping to manufacturing fully functional, end-use parts, particularly using metals. In order for these parts to be designed to function both safely and effectively, it is necessary to have a thorough understanding of the mechanical behavior of materials produced via the AM process.

This research focused on characterizing the high cycle fatigue (HCF) behavior of Inconel 718 produced via the Direct Metal Laser Sintering (DMLS) process. Material anisotropy in three orthogonal build orientations was evaluated along with the influence of the as-fabricated surface quality on fatigue performance. In addition to fatigue testing, surface roughness characterization, tensile testing, and fractography were performed on the additive manufactured specimens.

Measured fatigue strength of specimens built in horizontal orientations was found to be greater than that of specimens built in the vertical orientation. Furthermore, fatigue lives of specimens with a machined surface were significantly greater (10 to nearly 1000 times) than those of specimens left as-fabricated by the DMLS process. Results showed that specimens produced in an optimal build orientation for the particular loading condition and with improved surface quality via machining correlated well with published fatigue data for traditionally processed and polished Inconel 718 specimens.

Acknowledgements

A number of people provided invaluable guidance and assistance in supporting the completion of this thesis work for which I would like to extend my gratitude. I would first like to thank my advisor, Anil Saigal, for all of his guidance and insights in this effort. I'd like to thank Dr. Anthony DiCarlo for inspiring the thesis topic and providing guidance and encouragement while also serving on the review committee. Thank you to Gary Leisk for serving on the review committee. I'd like to thank Stratasys Direct Manufacturing, and in particular Andrew Carter, for their willingness to support this effort and for providing all additive manufactured materials for testing.

I would like to thank James Vlahakis for donating his time and patience in assisting with use of the profilometer. I would like to thank Christopher Nehme for his time and guidance on use of the Scanning Electron Microscope. Special thanks to Jim Hoffman and Vincent Miraglia, for providing any and all assistance I needed and answering endless questions, emails, and phone calls. I would like to thank all of my colleagues at MITRE, especially the MITRE Hardware Prototype Facility, for all of their support. And last but not least, I would like to give special thanks to my parents for their endless support and encouragement of my education, as well as all of my family and friends, especially Meghan O'Donnell, for all of their encouragement without which this work would not have been possible.

TABLE OF CONTENTS

1	Introduction.....	1
2	Background.....	5
2.1	Fatigue of Metals	5
2.1.1	Definition and Significance	5
2.1.2	Fatigue Fracture Characteristics.....	7
2.1.3	Fatigue Analysis.....	9
2.1.4	Fatigue Loading	11
2.1.5	Stress-Life (S-N) Diagram.....	13
2.1.6	Fatigue Testing.....	15
2.1.7	Factors Influencing Fatigue	18
2.2	Additive Manufacturing.....	21
2.2.1	Definition	21
2.2.2	Applications and Future	24
2.2.3	AM Technologies.....	27
2.2.4	Fusion Mechanisms in Powder Processes.....	30
2.2.5	Process Parameters for Powder Bed Fusion.....	31
2.2.6	Direct Metal Laser Sintering (DMLS).....	33
3	Literature Review.....	35
3.1	Fatigue of Additive Manufactured Inconel 718.....	35
3.2	Fatigue of Additive Manufactured Ti-6Al-4V	37
3.3	Fatigue of Other Additive Manufactured Metals	42
3.4	Tensile Behavior of Additive Manufactured Metals.....	44
3.5	Summary	46
4	Experimental Procedure and Materials	49
4.1	Experimental Procedure.....	49
4.2	Test Specimens	50
4.2.1	Tensile Test Specimens.....	52
4.2.2	Fatigue Test Specimens	54
5	Surface Characterization.....	58
5.1	Procedure	58
5.2	Results.....	60

5.3	Discussion	62
6	Tensile Testing.....	66
6.1	Procedure	66
6.2	Calculation of Parameters	69
6.3	Results.....	71
6.4	Discussion	74
7	Fatigue Testing.....	78
7.1	Procedure	78
7.2	Results.....	82
7.3	Discussion	83
7.3.1	Comparison with Published Fatigue Data.....	86
7.3.2	Determination of Material Constants	87
7.3.3	Comparison with Rule-of-Thumb Calculations	90
7.3.4	Comparison with Surface Roughness Correlation Factors	92
8	Fractography	95
8.1	Procedure	95
8.2	Tensile Fracture Surfaces.....	96
8.3	Fatigue Fracture Surfaces	99
9	Conclusions and Future Work.....	108
9.1	Summary of Results and Conclusions	108
9.2	Future Efforts	110
	Bibliography	112
	Appendix A.....	120
A1	As-Fabricated X Orientation Data	120
A2	As-Fabricated Y Orientation Data	121
A3	As-Fabricated Z Orientation Data.....	122
A4	Machined X Orientation Data	123
A5	Machined Y Orientation Data	124
A6	Machined Z Orientation Data	125

LIST OF TABLES

Table 4-1. DMLS Build Parameters	50
Table 4-2. Powder Composition	50
Table 5-1. As-Fabricated Tensile Specimen Surface Roughness	61
Table 5-2. As-Fabricated Fatigue Specimen Surface Roughness	61
Table 5-3. Machined Fatigue Specimen Surface Roughness	61
Table 6-1. Summary of Tensile Testing Results	74
Table 7-1. Applied Stresses in Fatigue Specimens	78
Table 7-2. S-N Relationship Constants	89
Table A-1. As-Fabricated X Orientation Specimen Dimensions	120
Table A-2. As-Fabricated X Orientation Specimen Fatigue Test Data	120
Table A-3. As-Fabricated Y Orientation Specimen Dimensions	121
Table A-4. As-Fabricated Y Orientation Specimen Fatigue Test Data	121
Table A-5. As-Fabricated Z Orientation Specimen Dimensions	122
Table A-6. As-Fabricated Z Orientation Specimen Fatigue Test Data	122
Table A-7. Machined X Orientation Specimen Dimensions	123
Table A-8. Machined X Orientation Specimen Fatigue Test Data	123
Table A-9. Machined Y Orientation Specimen Dimensions	124
Table A-10. Machined Y Orientation Specimen Fatigue Test Data	124
Table A-11. Machined Z Orientation Specimen Dimensions	125
Table A-12. Machined Z Orientation Specimen Fatigue Test Data	125

LIST OF FIGURES

Figure 2-1. Typical Fatigue Fracture Surface [8]	7
Figure 2-2. Fatigue Fracture Surface Patterns [8].....	8
Figure 2-3. Crack Nucleation Life versus Total Life [8]	10
Figure 2-4. Constant Amplitude Cyclic Loading.....	12
Figure 2-5. Typical S-N Curve for Steels [15].....	14
Figure 2-6. R.R. Moore Apparatus [8].....	16
Figure 2-7. Fatigue Factors for Surface Finish [8, 12].....	20
Figure 2-8. Typical Powder Bed Fusion Process [20]	28
Figure 3-1. Schematic of Referenced Build Orientations (Build Direction is Normal to Platform)	38
Figure 4-1. Build Orientations	51
Figure 4-2. DMLS Scan Strategy (Viewing Build Platform from Above)	52
Figure 4-3. Tensile Specimen Dimensions [mm]	53
Figure 4-4. Tensile Test Specimens.....	53
Figure 4-5. Fatigue Specimen Dimensions [mm]	54
Figure 4-6. X Orientation As-Fabricated Specimen	55
Figure 4-7. Z Orientation As-Fabricated Specimen.....	55
Figure 4-8. Horizontal Y Specimen Rough Underside.....	56
Figure 5-1. Zygo NewView 600S.....	58
Figure 5-2. Zygo MetroPro Software Display	60
Figure 5-3. Surface Topography of (a.) As-Fabricated and (b.) Machined Specimens ...	63
Figure 6-1. Instron 5800R Load Frame	66
Figure 6-2. Loaded Tensile Specimen with Extensometer	68
Figure 6-3. Determination of Modulus of Elasticity.....	70
Figure 6-4. Determination of Yield Strength.....	71
Figure 6-5. Load versus Extension Plot for All Specimens	72
Figure 6-6. Total Engineering Stress versus Strain Curves	73
Figure 6-7. Elastic Region of Engineering Stress versus Strain Curves	73
Figure 7-1. Specimen and Bearing Housing Assembly	79
Figure 7-2. Instron R.R. Moore Test Apparatus	79
Figure 7-3. Loading Harness and Weights.....	80
Figure 7-4. S-N Diagram for As-Fabricated and Machined Specimens	83

Figure 7-5. S-N Diagram with Curve-Fit Relationships	88
Figure 7-6. Predicted S-N Relationships vs. Test Data.....	91
Figure 7-7. Assessment of Surface Modifying Factors.....	93
Figure 8-1. Phenom Pro Desktop SEM [Photo courtesy of www.phenom-world.com]..	95
Figure 8-2. Images of (a.) X and (b.) Z Tensile Specimens [20X Magnification].....	96
Figure 8-3. Tensile Fracture Surfaces for (a.) X and (b.) Z Orientation Specimens	96
Figure 8-4. X Orientation Tensile Specimen SEM Images at (a.) 125X and (b.) 510X Magnification.....	97
Figure 8-5. Porosity in Z Orientation Tensile Specimen at (a.) 114X, (b.) 930X, and (c.) 2900X Magnification.....	98
Figure 8-6. Fracture Surfaces of Machined Specimens (a.) X7, (b.) Y8, (c.) Z9, and (d.) Z7 [20X Magnification].....	99
Figure 8-7. Fracture Surface Features [20X] (Machined Y8 Specimen)	100
Figure 8-8. SEM Images of (a.) Crack Initiation Site [113X] and (b.) Crack Progression Region [600X] (Machined Y8 Specimen)	101
Figure 8-9. SEM Images of (a.) Crack Initiation [125X] and (b.) Crack Progression [1000X] (Machined Z9 Specimen)	102
Figure 8-10. SEM Images of (a.) Transition Region [120X] and (b.) Final Fracture Region [600X] (Machined Z9 Specimen).....	102
Figure 8-11. Fracture Surfaces of As-Fabricated Specimens (a.) X3, (b.) Y3, (c.) Z4, and (d.) Z6 [20X Magnification]	103
Figure 8-12. SEM Images of (a.) Crack [125X] and (b.) Final Fracture [250X] (As- Fabricated Z4 Specimen)	105
Figure 8-13. SEM Image of Crack Propagation [120X] (As-Fabricated X3 Specimen)	105
Figure 8-14. SEM Images of (a.) Crack Initiation [114X] and (b.) Crack Propagation Regions [500X] (As-Fabricated Y3 Specimen)	106

1 INTRODUCTION

Additive manufacturing (AM) technology has developed significantly since its beginnings in the 1980s, with advancements in material capabilities, process techniques, efficiency, and part quality. Initial AM techniques involved the use of polymeric materials primarily to fabricate prototypes. As the technology has matured, processes have been developed to utilize metallic materials, and the application of AM has shifted from building prototype parts to manufacturing functional, end-use parts [1].

According to Gu et al. [2], “The next natural development of AM techniques is to produce complex shaped functional metallic components, including metals, alloys, and metal matrix composites (MMC’s) that cannot be easily produced by the conventional methods, in order to meet the demanding requirements from aerospace, automotive, rapid tooling, and biomedical industrial sectors.” This is evident in the aerospace industry, where General Electric has begun using AM to produce fuel nozzles for its jet engines [3]. Additionally, Space Explorations Technologies Corporation, or SpaceX, has recently announced that the engine chamber in its SuperDraco thruster was produced via AM, specifically utilizing Direct Metal Laser Sintering (DMLS) of the nickel super-alloy Inconel [4].

However, as AM becomes more focused on end-use parts, there is a need for better understanding of the AM processes and resulting material properties to ensure parts are properly designed for their applications and environments. As Gu et al. [2] additionally note, “Significant research and understanding are still required in the aspects of materials preparation and characterization, process

control and optimization, and theories of physical and chemical metallurgy for each AM process.”

While a survey of the literature yielded other efforts toward this end, as detailed in Chapter 3 of this thesis, there still remain many areas where further research is necessary. According to Brandl et al. [5] “In comparison to the static tensile performance, the fatigue performance of additive manufactured components is mostly disregarded.” Herderick [6] echoes the need for studying fatigue performance, while adding that “To date, there has been a relatively large body of work and focus on Ti-6Al-4V, but not as much on other alloys and metals.” Spierings et al. [7] add a specific area of need: “Laser-fabricated materials are known to be anisotropic and the effect of build orientation needs to be investigated in detail.”

It is the objective of the research herein to contribute to this effort by characterizing the fatigue behavior of Inconel 718, a nickel-based alloy known for its high-temperature and corrosion resistance. This alloy is popular in industries with relatively harsh environmental requirements, such as aerospace and nuclear.

The Inconel 718 specimens evaluated were produced via the Direct Metal Laser Sintering (DMLS) process. DMLS is a powder bed fusion additive manufacturing technique that was developed by EOS GmbH – Electro Optical Systems in the 1990s. The process, which will be further described in Chapter 2 of this thesis, utilizes a laser to melt and fuse metallic powder particles together, producing a part layer-by-layer.

The DMLS process results in a rough material surface, often requiring finishing operations to improve quality. This is particularly true on curved surfaces, where a “stair-step” effect takes place. As such, the research herein involved studying fatigue behavior of as-fabricated specimens, with surface quality characteristic of the process, as well as specimens produced via DMLS and subsequently machined to improve surface quality. While fatigue performance is highly dependent upon surface quality, a major benefit of the AM process is the ability to produce complex part geometries where internal cavities or other detailed features may not allow for secondary finishing operations. Hence, there is a need for designers and engineers to understand the impact of the as-fabricated surface quality on fatigue behavior.

Beyond machining to improve surface quality, no additional secondary processes were performed on the test specimens. In most applications, Inconel 718 is traditionally heat treated to anneal and age-harden, however this was not applied here. The need for secondary processes reduces the cost- and time-savings associated with AM. As such, the purpose of the effort herein was to evaluate the properties of the material in an as-fabricated state, without secondary treatments.

Additionally, specimens were evaluated in multiple build orientations. Since AM by definition builds parts layer-by-layer, different build orientations result in different material microstructure and, subsequently, possible anisotropy of material properties. This data can be used by designers and engineers to produce parts in the optimal orientation for fatigue performance in a particular application.

In addition to fatigue testing, surface roughness characterization was performed in order to quantitatively define surface quality. Tensile testing was performed to determine material yield strength in each orientation from which an appropriate fatigue loading would be derived. Finally, Scanning Electron Microscope (SEM) images of the fracture surfaces of both tensile and fatigue specimens were obtained and assessed to gain further insight into the material behavior.

Chapter 2 of this thesis begins by providing a background discussion on fatigue theory, methods of analysis, and testing as well as a discussion on additive manufacturing, particularly related to metals. Chapter 3 provides a review of related research efforts published in the literature regarding mechanical properties and fatigue behavior of additive manufactured metals. Chapter 4 includes an overview of the experimental procedure along with details on the materials and test specimens utilized. Chapters 5 through 8 include procedures, results, and discussions for the surface quality characterization, tensile testing, fatigue testing, and fractography, respectively. Finally, Chapter 9 concludes by tying together the results and proposing future research areas to further build upon this effort.

2 BACKGROUND

2.1 FATIGUE OF METALS

2.1.1 DEFINITION AND SIGNIFICANCE

Mechanical failures in metals are caused by some combination of load, time, and environment [8]. For example, a large static load may cause excessive deformation and subsequent failure of a material. Failure due to thermal creep exemplifies a combination of multiple factors, where a temperature environment causes deformation over a long time duration. Possible mechanical failure modes resulting from these factors for metals include yielding, brittle and ductile fracture, creep, buckling, corrosion, wear, and fatigue [8]. It is this final failure mode, fatigue, which is the focus of this research.

Fatigue can be simply defined as the failure of a material due to repetitive stress which may be above or below the yield strength [9]. The process is more precisely defined by the American Society for Testing and Materials (ASTM) [10]:

The process of progressive localized permanent structural change occurring in a material subjected to conditions that produce fluctuating stresses and strains at some point or points and that may culminate in cracks or complete fracture after a sufficient number of fluctuations.

The basic mechanism of fatigue involves three stages: crack initiation or nucleation, crack growth or propagation, and final fracture [9]. In the crack initiation period, a “small” crack is formed. As Stephens et al. [8] note, the

process beginning involves multiple micro-cracks that grow and combine to form this macro-level “small” crack. As for what constitutes “small,” Stephens et al. [8] assume 0.25 mm as a reasonable size, while Dowling [11] assumes an engineering size crack on the order of 1-5 mm. This definition is somewhat arbitrary and dependent on the particular application and inspection methods.

These cracks form due to high localized stresses at some stress concentration feature which subsequently leads to local plastic yielding, despite the fact that the nominal stress in the material may be below yield [12]. The stress concentrations occur at material discontinuities including macroscopic notch effects such as sharp corners, surface defects such as scratches, and microscopic level defects such as voids or inclusions, grain boundaries, or slip bands [8, 9, 11]. These cracks also tend to form at the material surface due to higher stress levels [8, 9].

Once a small crack is formed, the second stage involves growth of the crack under the continued fluctuating load, based on the principles of crack propagation and fracture mechanics, in what is known as the propagation period. Finally, the crack grows to a critical size where the remaining material cross section can no longer withstand the load and failure occurs. Combining the initiation and propagation periods results in the total fatigue life of the material, which ends with final fracture [13]

According to Stephens et al. [8], the literature suggests that 50% to 90% of all mechanical failures are fatigue failures, and the impact of these failures is significant. According to a study conducted in 1983, mechanical failures in the

United States resulted in a cost of \$119 billion, or approximately 4% of the gross national product [11]. Although not very recent, these numbers provide insight into the economic significance of fatigue. More important, however, is the risk of injury and loss of life resulting from these failures. There have been numerous examples of fatigue failures throughout history resulting in loss of life, often serving as motivation for breakthroughs in fatigue research. These include, among countless others, locomotive crashes, such as that of an Inter-City Express train in Germany in 1998 due to fatigue failure of a wheel rim, as well as multiple aircraft crashes, such as the incident on an Aloha Airlines Boeing 737 in 1988 involving fatigue failure of the fuselage [8]. Clearly fatigue is a significant failure mechanism that must be properly accounted for in engineering design.

2.1.2 FATIGUE FRACTURE CHARACTERISTICS

After typical fatigue failures, the fracture surfaces exhibit a few characteristic features. Figure 2-1 shows a typical fatigue fracture surface.

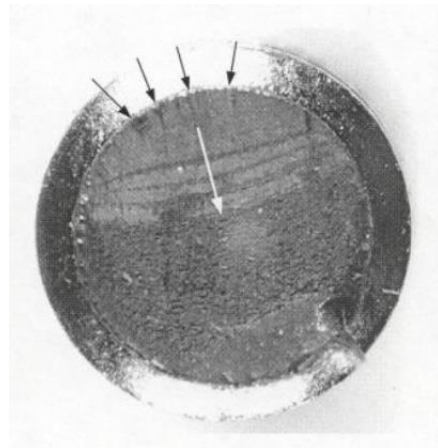


Figure 2-1. Typical Fatigue Fracture Surface [8]

The fracture surface is usually flat and relatively smooth around the crack origin, with a rougher surface indicating faster crack growth [11]. “Beach marks” are seen at a macroscopic level and are created by the changes in crack growth rate [8, 11]. At a microscopic level, striations are left by the crack after each cycle [9, 11]. Beach marks and striations represent the area of crack propagation and indicate the direction of crack growth. Finally, there is a final fracture region that may also include a shear lip, which is oriented at 45° and is characteristic of ductile metals.

Figure 2-2 below shows typical fracture surfaces for round bar specimens under rotating bending fatigue, which involves a rotating beam loaded such that it experiences cyclical bending stresses and is the case examined in this research.

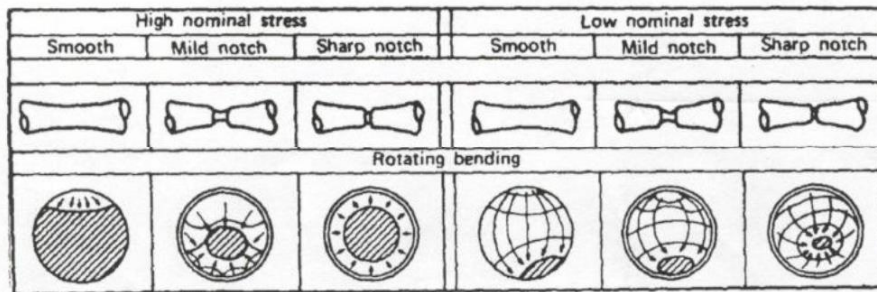


Figure 2-2. Fatigue Fracture Surface Patterns [8]

In Fig. 2-2, the arrows represent the “beach mark” region of crack growth, and the hatch marks represent the final fracture surface. As can be seen, for the smooth specimens, high nominal stresses lead to smaller areas of crack growth, as a larger load causes overload of the remaining cross-section more quickly. With low nominal stresses, the area of crack propagation is far greater.

2.1.3 FATIGUE ANALYSIS

The study of fatigue has its beginnings in the early to mid-1800s, primarily motivated by railroad accidents [14]. August Wohler of Germany was one of the most influential early researchers. In his study of fatigue failure of railroad axles, he conducted some of the earliest fatigue testing, and he designed the rotating-bending test along with other types of fatigue tests. He discovered and developed many concepts still used in fatigue analysis, including the stress-life (S-N) diagram and the endurance limit, which will be described in the following sections. [8, 14]

Three main approaches exist for analyzing fatigue: the stress-based method, the strain-based method, and the fracture mechanics method [11]. Wohler's work primarily falls under the stress-based approach to fatigue analysis, which is the oldest technique. Its basis is the stress-life (S-N) diagram, which is a plot of alternating stress versus fatigue life. This approach utilizes nominal stresses in the material, calculated based upon elastic stress versus strain relationships. Thus, this approach is best suited for situations when stresses are lower and strains are primarily elastic, and hence fatigue lives are longer [11, 13]. This is known as high cycle fatigue (HCF). Low cycle fatigue (LCF) occurs at higher stress levels and significant plastic strains, resulting in short lives, for which the stress-based approach is not well suited. The cutoff between LCF and HCF varies with material, but typically is between fatigue lives of 10^2 and 10^4 cycles [11].

The fatigue life plotted in the S-N diagram is the total life of the material, a combination of the crack initiation life and crack propagation life described

previously, and thus this method does not distinguish between crack nucleation and growth. This is shown in Fig. 2-3, where the “final fracture” line represents total life and a typical S-N diagram. [8, 13]

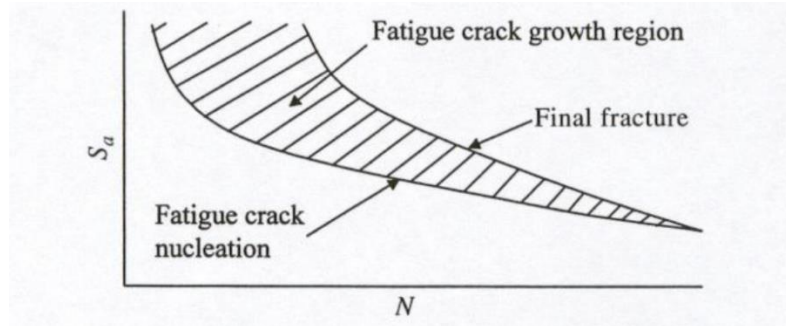


Figure 2-3. Crack Nucleation Life versus Total Life [8]

The stress-based approach relies on libraries of S-N diagrams from material testing to characterize the fatigue behavior of different materials, and as such is empirical in nature [13]. This is a widely used approach in fatigue design, and will be the focus of the analysis performed in this thesis.

The strain-based approach, on the other hand, allows for the consideration of true stress versus strain behavior at the localized high stress areas by accounting for plastic strains. Therefore, this method can be used at lower lives, in the LCF region, where large plastic strains are involved. This method can also be used in the HCF region where little plasticity is involved, thus overlapping with the stress-based approach. If strains are mostly elastic, there is no benefit to using the strain-based approach in lieu of the stress-based. This method only accounts for crack initiation life (in contrast to the total life of the stress-based approach), and its basis is the strain-life (ϵ -N) diagram, similar to the S-N diagram. [13]

The final approach to fatigue analysis is the fracture mechanics approach, which is the only approach to involve detailed consideration of fatigue cracks. This approach focuses on determining the crack propagation life and, as such, it can be combined with the strain-based approach to determine a total fatigue life of a material, as depicted in Fig. 2-3. This approach is based in linear elastic fracture mechanics (LEFM) and requires assumptions for stress intensity factors and initial crack sizes, which are often difficult to estimate. [13]

2.1.4 FATIGUE LOADING

As mentioned in defining fatigue, the process involves fluctuating, cyclic loading as opposed to static loading. The simplest loading to consider is constant amplitude loading. In reality, environmental loading can be variable amplitude, or even completely random, and techniques do exist for assessing these conditions. However, constant amplitude loading is typically utilized in testing materials to characterize their fatigue behavior, and this characterization can be utilized in assessing response to real environments [8, 11]. This discussion will focus on constant amplitude loading as that is the case that applies to the testing herein.

Figure 2-4 shows a constant amplitude cyclic load.

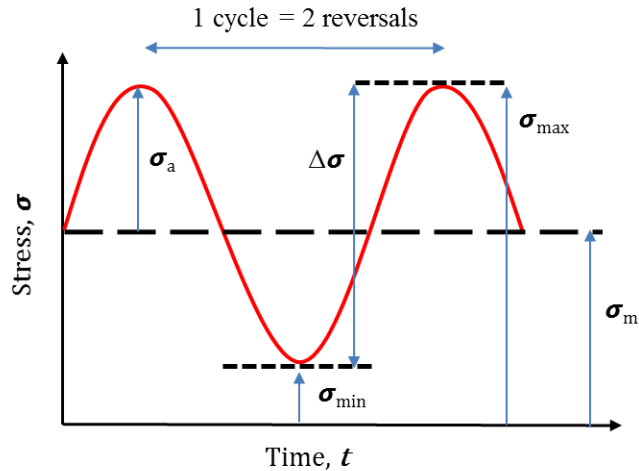


Figure 2-4. Constant Amplitude Cyclic Loading

Equations (1) to (4) define the stress range $\Delta\sigma$, stress amplitude or alternating stress σ_a , mean stress σ_m , and stress ratio R . [11]

$$\Delta\sigma = \sigma_{max} - \sigma_{min} \quad (1)$$

$$\sigma_a = \frac{\Delta\sigma}{2} = \frac{\sigma_{max} - \sigma_{min}}{2} \quad (2)$$

$$\sigma_m = \frac{\sigma_{max} + \sigma_{min}}{2} \quad (3)$$

$$R = \frac{\sigma_{min}}{\sigma_{max}} \quad (4)$$

As can be seen, mean stresses on a material shift the point around which the alternating stress fluctuates and influence the fatigue behavior of a material.

Assessment of fatigue with mean stresses involves the use of Haigh diagrams to plot alternating versus mean stress for a given life, as well as the use of different empirical relationships to model these effects. As the testing in the research herein does not involve mean stresses, these techniques are not further detailed.

[11, 13]

The case of zero mean stress results in $\sigma_{max} = -\sigma_{min}$, thus using Eqn. 4 this results in an R ratio of -1. This is known as fully reversed loading, since the maximum tensile alternating stress is equivalent to the maximum compressive alternating stress [11]. This case describes the testing completed as part of the research herein.

2.1.5 STRESS-LIFE (S-N) DIAGRAM

As mentioned, the stress-based approach is predicated upon the S-N diagram, also known as the Wohler diagram [13]. In order to create an S-N diagram for a material, load-controlled fatigue testing is performed from which a number of cycles to failure is recorded. An alternating stress level is calculated using linear elastic relationships based on the loading applied. Conducting a series of these tests across different stress levels and plotting alternating stress versus cycles to failure results in an S-N diagram. These diagrams are typically plotted with the number of cycles on a logarithmic scale, because fatigue life increases significantly with decreasing stress levels. [11, 13]

Below a certain stress level, known as the fatigue or endurance limit, some materials exhibit what appears to be an infinite life, although in reality this is some significantly high number of cycles [11, 13]. As Askeland and Phule [9] define it, below this limit there is a 50% probability fatigue failure will not occur. The S-N curve for these materials thus has a “knee” and plateaus at this endurance limit stress value. Ferrous materials tend to exhibit this behavior [12], and primarily body-centered cubic (BCC) steels [13] display these limits. Figure 2-5 depicts a typical S-N curve for steels.

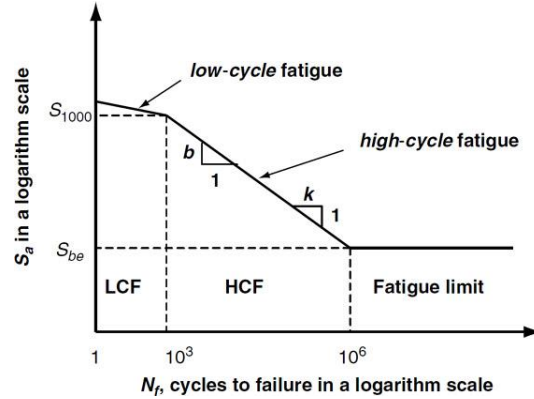


Figure 2-5. Typical S-N Curve for Steels [15]

Most non-ferrous alloys, such as aluminum, do not exhibit a true endurance limit, and as such their S-N curves do not plateau like those of steels. For these materials, the fatigue strength at 10^8 or 5×10^8 cycles is often considered as an endurance limit. [12, 13]

For S-N data displaying a linear trend on a log-log plot (under completely reversed loading), the data can be fit with the power relationship shown in Eqn. (5), which is known as Basquin's equation [8, 11].

$$\sigma_a = AN_f^B = \sigma_f'(2N_f)^b \quad (5)$$

In this equation, σ_f' is a constant approximately equal to the true fracture strength of the material, which is a value slightly above ultimate tensile strength for ductile metals [11], and b is the slope of the S-N curve, typically ranging from -0.05 to -0.2 for un-notched specimens [8]. The $2N_f$ term denotes the number of reversals to failure, where 1 reversal is equal to $\frac{1}{2}$ cycle [13]. Values for these constants are determined empirically and can be found in the literature for various materials [11].

For steels, empirical relationships have been developed to relate fatigue behavior to tensile properties [13, 15]. For steels with an ultimate strength below 1379 MPa [200 ksi], the endurance limit can be taken to be approximately 50% of ultimate strength, where this ranges between 35% and 60% [8, 13]. Additionally, the fatigue strength at 1000 cycles can be assumed to be equivalent to 90% of ultimate strength [13]. Then a power law relationship can be applied to estimate the S-N curve between 10^3 and 10^6 cycles as shown in Eqn. (6) to Eqn. (8) [13].

$$\sigma = 10^C N^b \quad (6)$$

$$b = -\frac{1}{3} \log_{10} \frac{\sigma_{1000}}{\sigma_e} \quad (7)$$

$$C = \log_{10} \frac{(\sigma_{1000})^2}{\sigma_e} \quad (8)$$

In these equations, N is cycles to failure, σ_{1000} is fatigue strength at 1000 cycles, and σ_e is the fatigue endurance limit. Substituting in the empirical relationships and the ultimate strength values for the given material allows for the development of a predicted S-N curve. While these relationships have only been shown to hold true for steels, they are used in the research herein as a tool for comparison.

2.1.6 FATIGUE TESTING

Various types of fatigue tests exist, with different loading conditions and material forms. This might involve some combination of bending, tensile, or torsional loading and material in various forms such as sheet or bar. Additionally, fatigue tests can be load-controlled or strain/displacement controlled. Development of S-

N diagrams in the stress-based approach is performed using load-controlled testing [11].

One of the oldest test methods is rotating-bending fatigue testing, which dates back to Wohler in the mid-1800s [11]. This type of test can be conducted on an R.R. Moore rotating-beam system, which was utilized in the research herein. In this apparatus, a cylindrical test specimen is fit into two bearings, one at each end, from which a load is hanged. Outer bearings on each end act as supports. The specimen assembly is tied to a motor via a coupling, and a revolution counter is used to record number of cycles. A diagram of a typical R.R. Moore apparatus is shown in Fig. 2-6. [11, 12]

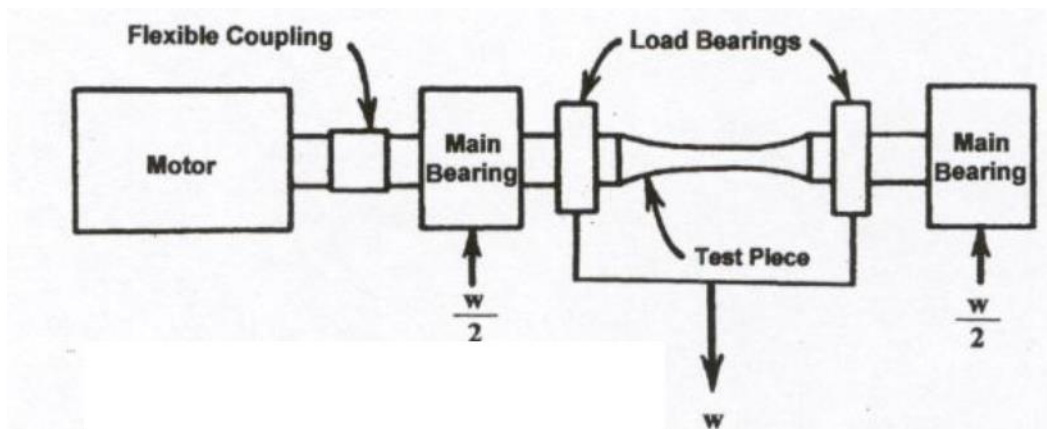


Figure 2-6. R.R. Moore Apparatus [8]

The rotating-beam system induces four-point bending on the specimen, which results in a pure bending condition with zero transverse shear load [12]. With each rotation, the specimen surface fluctuates between maximum tensile bending stress and maximum compressive bending stress. This results in fully reversed loading as described previously, characterized by the stress ratio $R = -1$ [11].

This testing is load-controlled, meaning amplitude of the applied force is constant (achieved by hanging a particular amount of weight throughout the test). Stress levels in the specimen are thus calculated for the given load, based upon elastic stress-strain relationships. Surface stresses could not be calculated in this manner if nominal plastic deformations and strains were induced in the specimen.

Therefore, the loading applied should be such that the induced stress is within the elastic range and below material yield strength. For assessing higher stress levels, the strain-based approach and strain-controlled testing should be employed. [11]

For the rotating-beam test, the maximum surface stress at the center of the specimen can be calculated from Eqn. (9), which is derived from four-point bending.

$$\sigma = \frac{16WL}{\pi d^3} \quad (9)$$

In this equation, L is set at 4 inches for the particular test system used herein, d is the minimum diameter of the reduced section of the fatigue specimen (0.2 inches), and W is the applied loading. A 10 lb effective weight must be included in the calculation, in addition to the applied loading, to account for the weight of the yoke and the weight pan. [16]

One type of specimen utilized in this testing is a round bar with a gradual taper to a minimum diameter center section. The gradual taper ensures there is no geometric stress concentration and that the maximum stress will be induced at the center minimum diameter. Thus, this minimum diameter is used in the stress

calculation in Eqn. (9). Notched specimens may also be utilized depending on the type of testing being performed. [11]

As mentioned, a series of these tests performed at different stress levels allows for the development of an S-N diagram. Because of the nature of fatigue failure, originating at material defects that vary randomly between specimens, there is a significant amount of scatter in test data [8, 11, 12]. According to Juvinall and Marshek [12], for a given fatigue strength in controlled testing, scatter in resulting fatigue lives can be as high as 10 to 1. This scatter in the data also tends to increase for longer lives and lower stresses [11].

2.1.7 FACTORS INFLUENCING FATIGUE

Beyond the impact of mean stresses, variable amplitude loading, and notches which have already been mentioned, there are other aspects that influence fatigue behavior of a material. These include specimen size, type of loading, temperature, surface finish, surface treatments, residual stresses, frequency of loading, environment, and microstructure.

Since fatigue testing typically involves an ideal scenario (mirror-polished, fully reversed bending, lab environment, particular size specimen, etc.), empirical factors have been developed in order to account for some of these effects [13].

While ideally fatigue testing would be performed under conditions simulating the actual service environment, these factors provide a rough estimate of the impact of these different effects. Both Juvinall and Marshek [12] and Bannantine et al. [13] present equations for applying modifying factors to S-N data to determine endurance limit in the form of Eqn. (10).

$$S_e = S_e' C_{size} C_{loading} C_{surface} C_{temperature} \quad (10)$$

In this equation, S_e' is the endurance limit of the mirror-polished specimen resulting from an R.R. Moore test. The C factors are empirical factors that modify the endurance limit for the various conditions. This equation was developed specifically for endurance limit, however it can be utilized across the entire S-N curve resulting in a conservative prediction. [13]

In general, the size factor accounts for the steepness of stress gradients in various size test specimens, the loading factor relates bending to other loading scenarios such as torsion or tension, and the temperature factor accounts for reduction of endurance limit at high temperatures [13]. Since the testing involved as part of this thesis involves typical round bar specimens under fully reversed bending at room temperature, most of these C factors will be equal to unity, except for that related to surface finish, which is an area of focus in this research.

Surface finish and other surface effects, such as residual stresses, have a significant influence on material fatigue behavior. Typical manufacturing processes result in varying surface texture, roughness, and random imperfections such as scratches which may all act as stress concentration sites for fatigue cracks. These processes also result in residual stresses within the material. Tensile residual stresses lower fatigue resistance while compressive residual stresses improve it. Thus surface treatments that induce compressive residual stresses, such as shot peening, are beneficial whereas nickel or chrome plating, which induce tensile residual stresses, are detrimental. [11, 12, 13]

As described above, a reduction factor is available to apply to test data for polished specimens to estimate the impact of surface effects. Stephens et al. [8] and Juvinall and Marshek [12] present the plot shown in Fig. 2-7 to determine this factor for surface quality, $C_{surface}$, for use in Eqn. (10). It should be noted that the factors in this plot account for both surface finish resulting from the given process as well as any other effects, such as residual stresses.

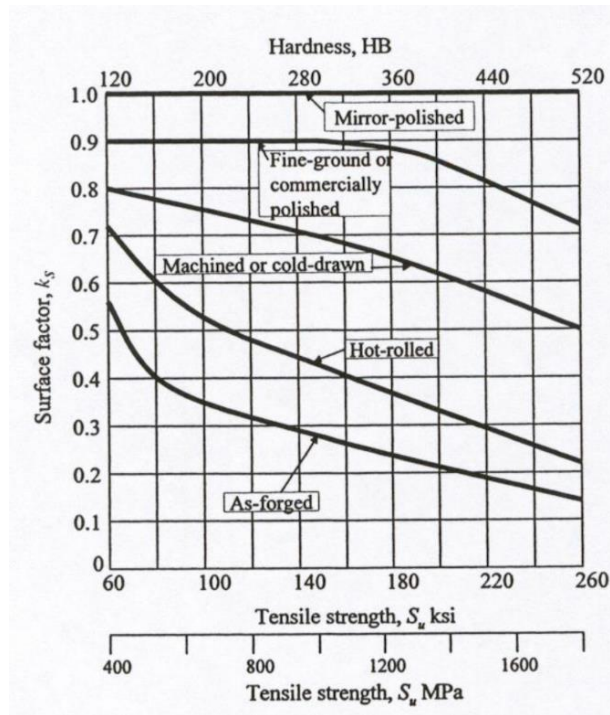


Figure 2-7. Fatigue Factors for Surface Finish [8, 12]

Additionally, Bannantine et al. [13] presents a separate plot which provides factors based on surface roughness values.

Other factors impacting fatigue behavior, for which empirical values are not readily available, include frequency of loading, environment, and microstructure. Higher frequency loading leads to an increase in temperature as well as higher strain rates, which both impact the material fatigue behavior [8]. According to

Stephens et al. [8], frequencies less than 200 Hz in tension or bending fatigue tests typically have minimal effect on S-N behavior of metals.

Another important factor is environment. Corrosive environments lead to the formation of corrosion pits, and hence local stress concentrations, on a material surface [13]. Additionally, environments such as salt atmosphere may accelerate crack growth and lower fatigue life [11].

Material microstructure also influences fatigue behavior. As previously mentioned, microstructural discontinuities, such as inclusions or voids, act as crack initiation sites due to stress concentrations. Additionally, smaller grain sizes typically improve fatigue life by providing resistance to crack growth.

Anisotropy in grain structure can also impact fatigue, where fatigue life is greater when stresses are aligned with the elongated grain direction. [8, 11]

2.2 ADDITIVE MANUFACTURING

2.2.1 DEFINITION

ASTM defines additive manufacturing as “a process of joining materials to make objects from 3D model data, usually layer upon layer, as opposed to subtractive manufacturing methodologies” [17]. It is commonly referred to as 3D printing, although, according to ASTM [17], the term “3D printing” refers to a particular additive process involving the use of printer technologies, such as a print head or nozzle. Additive manufacturing (AM) is the general term that will be utilized to describe the process herein.

According to Bourell et al. [18], the earliest beginnings of AM can be traced to developments in the late 1800s in both topography and photosculpturing, in which maps and sculptures were built layer-by-layer. However, modern AM processes have their roots in research and patents beginning in the 1950s. In particular, a patent by Pierre Ciraud in 1971 describes a process for using a beam of energy to solidify a powdered material in order to build up a geometry, resembling modern metal AM processes [18, 19]. It was in the 1980s that AM was first commercialized by Charles Hull with his development of the stereolithography process for polymers and subsequent formation of 3D Systems Inc [19].

In contrast to conventional “subtractive” manufacturing techniques such as milling or drilling, in which material is removed in order to create a part, AM processes build parts up in layers. This results in less excess raw material being utilized, and subsequently lower material costs. In addition, the process allows for complex geometries that are either not easily accomplished or not possible with subtractive techniques. This includes internal cavities as well as lattice structures or integrated honeycomb structures, which can be used to optimize the strength-to-weight ratio of a design. [1, 2, 19, 20, 21]

There is no need for development of special tools or fixtures and associated long lead times with AM, and it is cost-effective for small-scale production, even single parts. In addition, design changes can be implemented quickly to manufacture a new part. These unique aspects make it ideal for rapid prototyping, which was the primary application of the technology, particular with the early polymer AM processes. [1, 2, 19, 20, 21]

However, AM is not without its disadvantages. AM can be cost-prohibitive for large production quantities, which limits its ability to entirely replace traditional manufacturing techniques. Also, the number of available materials is relatively small at this point, compared with traditional techniques. Furthermore, according to Horn and Harrysson [21] “The freedom afforded by this technology also brings with it an entirely new set of challenges and constraints. Consider the resolution associated with the thickness of discrete layers, the surface roughness of components, poor dimensional accuracy, minimum feature sizes (i.e. thin walls, ribs, slots, etc.), and anisotropy associated with different part orientations.” Until processes are further improved, secondary finishing operations are frequently necessary to obtain the desired part quality. Variation in process parameters also impacts consistency of part quality along with material microstructure and mechanical properties, which is a concern in producing parts for end-use. [1, 2, 21]

Characterizing material properties and how they relate to specific processes and parameters remains a research need for AM [2]. As Herderick [6] notes, there is a “need for a comprehensive material property database” for AM materials. In particular “Studies of the effect of processing parameters on dynamic loading in high and low cycle fatigue...will be important to fully understand the performance of AM parts in service like conditions” [6]. Adding to this understanding of AM material properties, and in particular high cycle fatigue behavior, is the aim of the research herein.

2.2.2 APPLICATIONS AND FUTURE

As mentioned, early AM systems were primarily used for rapid prototyping. Models could be made quickly and cost effectively to evaluate form, fit, and function of a part throughout the development phase. However, as AM processes evolved and new materials were introduced, the potential applications increased. While prototyping is still an important use of AM, Guo et al. [1] state that “Currently, the direct fabrication of functional end-use products has become the main trend of AM technology.” This judgment is echoed by Gu et al [2], specifically emphasizing the focus on metals: “The next natural development of AM techniques is to produce complex shaped functional metallic components...Actually, components produced by AM are no longer used merely as visualization tools, but to be used as real production parts (i.e., end-use products) which have basic mechanical properties meeting the industrial requirements.”

AM is especially suitable for customized or complex low volume production [1], making it ideal for certain industries. According to Gibson et al. [20], the aerospace, automotive, and medical industries have been key in propelling AM innovations. The automotive and aerospace industries benefit from the ability to produce complex geometries with relative ease (thus allowing for weight-reduction features to be incorporated into part designs) as well as the rapid prototyping ability which significantly reduces cost and time in the development phase.

Within the medical industry, the customization possible with AM for individual patients has made the technology very popular since its beginnings. The first applications involved using AM to generate 3D models of a patient's anatomy based on medical imaging data to plan or practice surgical procedures. As AM processes and materials improved, orthopedic and dental implants as well as prosthetics have become a major application of AM. In addition, AM is used for manufacture of custom medical devices, particularly hearing aids. More recently, it has been used to develop scaffolds for tissue engineering and, with the maturation of biomaterials, to print living cells, even organs. [1, 20, 21]

Across many industries, the use of AM in rapid tooling has also been a major application. AM can be utilized to produce injection molding inserts, patterns for investment casting, molds or cores for composite layups, or even jigs or template tools to assist in assembly or inspection of parts [20]. Benefits to using AM include speed and cost, as well as the ability to quickly produce new tooling to accommodate part changes. This represents an indirect method of utilizing AM to produce end-use parts, while the current trend is shifting towards directly producing these functional parts without the need for further processing.

Of particular interest is the aerospace industry, as Inconel 718, the material studied herein, is a high performance alloy commonly used in this industry. According to Horn and Harrysson [21], the ratio of the mass of raw material needed to manufacture an aerospace part to the mass of the final part can be as high as 20:1, while with AM this ratio approaches one. An article in the Economist [22] mirrors this sentiment, stating that additive manufactured parts

“can be as strong as a machined part but use only 10% of the raw material.” The economic benefits are thus clear to growing AM for aerospace applications.

Additionally, the ability to produce complex geometries, such as intricate internal cooling passages, greatly benefits this industry.

Examples of AM applications in the aerospace industry are abundant. According to General Electric’s website [23], 100,000 additive parts will be manufactured by GE Aviation by 2020. This mainly accounts for an engine fuel nozzle that is currently being produced via AM. Utilizing AM allowed for a more efficient nozzle with significant weight and cost reductions, while being optimized for life [20]. Additionally, Space Explorations Technologies Corporation (SpaceX) has recently announced that the engine chamber in its SuperDraco thruster is produced via AM of an Inconel alloy, as used in the research herein [4]. Certain AM processes have also been used to repair aircraft engine parts [1].

AM has grown significantly since its inception in the 1980s and is evolving beyond simply a process for manufacturing prototypes or visual aids [21].

According to an article in Metal Powder Report [24], the AM market is expected to grow at a “CAGR of 23% from 2013 to 2020, and reach US\$8.41 billion in 2020.” As mentioned, there are multiple areas where AM needs to further develop and improve in order to continue its growth and application areas. These include, among others: standardization of processes, materials, and design guidelines; improvement of processes as far as part accuracy, quality, build volume, build times, number of materials, etc.; and a more detailed theoretical

understanding of the impact of process parameters and the material bonding mechanisms [2, 21].

2.2.3 AM TECHNOLOGIES

The maturation of AM has involved the development of various techniques to better accomplish the process of building parts in a layer-wise manner. There are many ways these processes have been grouped and classified in the literature, including by build material (polymer, metal, composite, ceramic) [25, 26], the state of the raw material in the process (liquid, filament, powder, or solid) [1, 25], or, for metals, whether the process directly or indirectly produces an end part [1].

ASTM F2792 [17] defines process categories in order to “provide a structure for grouping current and future AM machine technologies.” These categories are: binder jetting, in which powder materials are bonded via liquid bonding agents; directed energy deposition, in which an energy source melts and fuses a material as it is deposited; material extrusion, where material is deposited through a nozzle; material jetting, in which material droplets are deposited; powder bed fusion, in which an energy source fuses powdered material; sheet lamination; and vat photo-polymerization, in which liquid photopolymer is cured via light. [17]

There are many processes that fall into the categories defined above, with different names and variations specific to the company or organization that developed them. As mentioned, polymer AM processes comprised the first techniques developed, and these include such processes as stereolithography (SLA), fused deposition modeling (FDM), selective laser sintering (SLS), digital light processing (DLP), and 3-dimensional printing (3DP). These polymer

processes have a range of methods for binding material, including sintering a powder polymer via a laser or heat source, extruding a melted polymer filament, binder jetting into a polymer using inkjet printer techniques, or curing a polymer using UV, laser, or digital light.

Since the processes utilized in the AM of metals are both the current focus of the industry as well as pertinent to the research herein, these will be discussed in further detail. The majority of metal AM processes and research tend to fall under the directed energy deposition and powder bed fusion categories defined by ASTM. In general for metals, an energy source, such as a laser, is used to either sinter or fully melt metal powder particles.

Powder bed fusion techniques may vary slightly depending on the particular process, however the overall concept is the same. The basic concept is illustrated in Fig. 2-8.

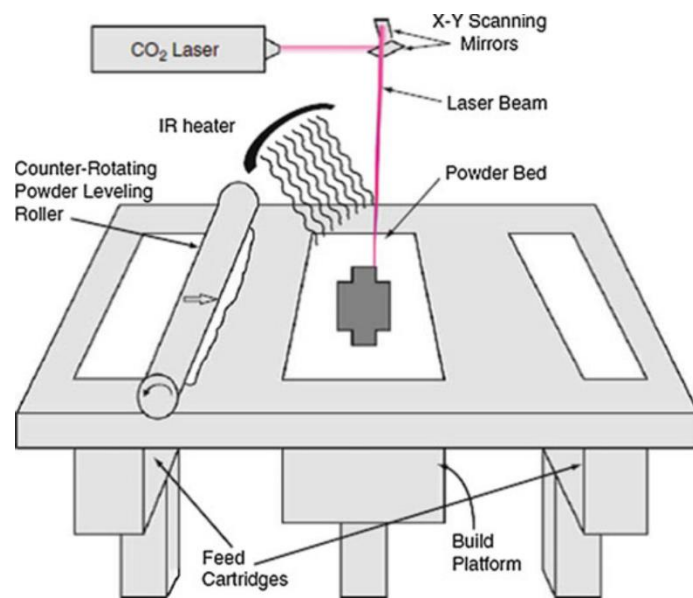


Figure 2-8. Typical Powder Bed Fusion Process [20]

Powder particles of the build material are spread across the build platform into a smooth “bed”, such as by a roller. The build area is located within an enclosure that is filled with an inert gas. An energy source, such as a laser, is used to fuse the powder particles via a sintering or melting mechanism, which will be discussed below. The energy source is able to be focused in order to trace out the cross section and area of the particular layer of the part.

Once a layer is complete, the build platform is lowered and a new layer of powder is introduced and subsequently fused. The part is typically fused to the build plate to prevent warping, which requires removal after the process. Additionally, while the loose powder in the bed provides some support, support structures are often necessary for overhang features or to prevent warping. Some examples of processes that fall under the powder bed fusion category are Selective Laser Sintering (SLS), Direct Metal Laser Sintering (DMLS), Selective Laser Melting (SLM), and Laser Cusing, which all utilize a laser as an energy source. Another popular powder bed fusion process, Electron Beam Melting (EBM), utilizes an electron beam as an energy source. [20]

Directed energy deposition accounts for the other large portion of metal AM processes. This method differs from powder bed fusion in that the powder material is not spread in the build area, but rather it is melted as it is deposited using a focused thermal source, such as laser or electron beam [20]. Directed energy deposition processes allow for adding material to existing parts, thus they can be used for repairing parts in addition to creating new ones [20]. Some commercial variants of directed energy deposition include Laser Engineered Net

Shaping (LENS), Laser Consolidation (LC), and Direct Metal Deposition (DMD). Additionally, processes exist where the raw material is fed in a wire form as opposed to powder, such as Electron Beam Additive Manufacturing (EBAM) by Sciaky Inc.

Other AM techniques have been developed for metals that do not use beam energy sources as in the powder bed fusion and directed energy deposition techniques described. These include Ultrasonic Consolidation by Solidica, which utilizes ultrasonic energy to bind sheet metal together. Metals can also be printed using a binder jetting technology (3DP), as by the company ExOne, in which a liquid binder is sprayed onto powder particles and solidifies to form a layer.

2.2.4 FUSION MECHANISMS IN POWDER PROCESSES

There are different mechanisms by which powder particles can be fused in both powder bed fusion and directed energy deposition processes, which are sometimes used as a way to group various AM technologies as well. Detailed explanations of these mechanisms are provided by Kruth et al. [27] as well as Gibson et al. [20]. They include solid-state sintering, liquid phase sintering/partial melting, full melting, and chemically induced binding [20, 27].

Solid state sintering involves diffusion between powder particles at temperatures below the melting point which results in physical “necking” between the particles. This diffusion process is slow, however, and hence is not widely utilized in AM processes [20, 27].

Liquid phase sintering occurs when a portion of powder particles melt while the rest remain solid, and the molten powder binds together the solid particles. This may involve the use of a separate “binder” material with a lower melting point. This binder may be present as separate powder particles, a coating on the primary particle, or as part of a composite particle [20]. The binder may or may not be removed in a secondary operation. Liquid phase sintering can also occur without a binder, by inducing a partial melting of a single powder material. Liquid phase sintering results in porous parts that may require secondary densification processes, however is quicker than fully melting the powder. [20, 27]

Full melting is, as the name suggests, complete melting and fusing of the powder particles together, resulting in near 100% dense parts. This mechanism results in re-melting of layers just below the current layer due to the high energy density [20]. Full melting has been made possible advancements in laser and energy source technologies. One drawback of full melting is it results in high residual stresses within a part [27].

Finally, chemically induced binding, more popular in ceramics [20], involves binding powder as a result of chemical reactions between two material particles or a material and a gas. [20, 27]

2.2.5 PROCESS PARAMETERS FOR POWDER BED FUSION

According to Gibson et al. [20], there are four major categories of process parameters related to powder bed fusion processes: laser parameters, scan parameters, powder parameters, and temperature parameters. The interaction of these parameters significantly influences the resulting material properties and part

quality. Equipment manufacturers such as EOS have worked to optimize the combination of these parameters for particular materials and often the specific details are proprietary. [20]

Laser parameters include laser power and spot diameter, which impact the energy imparted to the powder. Scan parameters may include scan speeds and scan patterns used during the build. Scanning of the outer contour is typically performed first, followed by scanning the remainder of the cross-sectional area for a given layer. Various patterns are used when scanning within the area, including stripes, which can be rotated every layer, or dividing the area into a grid within which random stripe patterns are used. Scan strategies impact residual stresses induced within the material, and more randomization in scan patterns may reduce residual stress levels and directionality. [2, 20]

Powder properties include such things as size and shape which impact how the powder melts during the process. Additionally, chemical composition and handling of the powders is important to ensure no contamination occurs. Specific to the powder bed fusion processes, loose powder remaining after a build is typically recycled and reused. The raking process and the build environment can affect the powder, such as modifying the shape or roughness, and thus will influence the properties of future builds. Finally, temperature parameters, such as temperature of powder or of the build plate, can impact final part characteristics. [20]

One common value used to characterize the impact of some of these parameters is volumetric energy density. Density of AM produced parts is a key property that influences mechanical behavior, and the energy density imparted to the powder particles is closely related to final material density. Equation (11) defines the volumetric energy density, VED , (in units of J/mm^3). [2]

$$VED = \frac{P}{vhd} \quad (11)$$

In Eqn. (11), P is laser power, v is laser scan speed, h is hatch or scan spacing, and d is layer thickness. If VED is too low or too high, pores may be formed in the part. Thus there is an optimal window, depending on the particular material being processed, which should be targeted. [2]

2.2.6 DIRECT METAL LASER SINTERING (DMLS)

The Direct Metal Laser Sintering (DMLS) process will be utilized in fabricating the parts for the research herein. DMLS is defined in ASTM F2792-12a [17] as “a powder bed fusion process used to make metal parts directly from metal powders without intermediate “green” or “brown” parts; term denotes metal-based laser sintering systems from EOS GmbH – Electro Optical Systems.” The process was developed by EOS in the early 1990s, with the first commercial system available in 1995 [19]. EOS, with its DMLS process, is currently the “biggest player in the 3D metals printing industry.” [28]

As mentioned, DMLS is a powder bed fusion process and thus involves the general steps described in the Section 2.2.3 and is impacted by process parameters as described in Section 2.2.5. The system utilized herein was an EOSINT M 280.

This system contains either a 200 W or 400 W Ytterbium (Yb)-fiber laser, and is filled with either nitrogen or argon, depending on the material being processed [29]. Specific process parameters used in building the specimens for this research are detailed in Chapter 4.

Despite the registered name of the process containing the term “sintering,” current iterations of DMLS systems, with more advanced lasers, result in full melting of powder particles as described in Section 2.2.4. Gu et al. [2] show that DMLS falls under laser sintering in reference to the EOSINT M 250 system which utilize a CO₂ laser, while it belongs to the laser melting category for the EOSINT M 270/280 with fiber laser.

3 LITERATURE REVIEW

A review of the literature was completed in order to uncover similar efforts toward characterizing additive manufactured metals and any resulting data or conclusions that could be used for comparison with the research herein. The following sections discuss the pertinent findings based on topic.

3.1 FATIGUE OF ADDITIVE MANUFACTURED INCONEL 718

The initial literature review focused on finding any published research characterizing fatigue behavior of the same material, additive manufactured Inconel 718. Scott-Emuakpor et al. [30] assessed the high-cycle fatigue behavior of plate-type DMLS specimens (produced on an EOSINT M 280 system) under vibration-based bending on a shaker table. Specimens in this study were provided by two separate vendors, both in the same build orientation, and with different process parameters, some of which were proprietary and unknown. One vendor subjected specimens to post-build aging, stress relieving, and Hot Isostatic Press (HIP) while one vendor performed no post-build treatments. Average surface roughness values of the as-built specimens were provided, which compared favorably to those measured experimentally herein (as will be discussed in Chapter 5). All specimens used in testing were polished to improve surface quality.

The results of the fatigue testing by Scott-Emuakpor et al. [30] showed good agreement between the DMLS specimens produced by each vendor and published cold-rolled Inconel 718 fatigue data between 10^5 and 10^6 cycles. However,

correlating this difference to particular process parameters was not possible due to the limited knowledge of the vendor proprietary parameters. The fatigue results for the specimens that did not undergo post-build treatments were used for comparison with the results obtained herein (Chapter 7).

A study by Amsterdam et al. [31] involved fatigue testing of Inconel 718 material fabricated via a different AM process, Laser Engineered Net Shaping (LENS). The specimens used in this study were machined from a larger component and also underwent a heat treatment process post-build. Fatigue testing was conducted with specimens from one build orientation. The authors concluded that the presence of pores and a lack of bonding between build layers reduced the fatigue performance of the additive manufactured Inconel 718, however it still compared favorably to published data for annealed and aged sheet material. The research herein differs in that, along with the particular AM process, the specimens are tested in both as-fabricated and machined configurations as well as different build orientations, without any secondary processing or heat treatments.

Kirka et al. [32] performed high cycle fatigue testing on Inconel 718 specimens produced via the EBM process. Specimens were tested as-built in both horizontal and vertical build orientations, as well as after heat treatment and after a HIP process. Results showed that, on average, the EBM specimens underperform both cast and forged Inconel 718 data, even with post-process treatments. The authors attribute this to the presence of micro-porosity in the material, and in one specimen subjected to a longer HIP treatment the fatigue life approaches that of wrought material. Additionally, material anisotropy is observed related to build

orientation, with the as-built horizontal orientation results approaching the wrought material as well.

3.2 FATIGUE OF ADDITIVE MANUFACTURED TI-6AL-4V

Much of the work discovered in surveying the literature was focused on characterizing the performance of other additive manufactured metals, in particular Ti-6Al-4V. This finding is echoed by Herderick [6], who notes that there has been a “relatively large body of work and focus on Ti-6Al-4V, but not as much on other alloys and metals.” This further supports the need for research into other material capabilities, such as Inconel 718.

These efforts have focused on Ti-6Al-4V produced by a variety of AM processes, including directed energy deposition methods. For example, Wang et al. [33] performed fatigue testing on specimens produced via wire and arc additive manufacturing (WAAM). The majority of the additive manufactured specimens showed significantly higher HCF lives than those of forged bar specimens. For the few that did not exceed the forging, the difference was attributed to pores near the specimen surface caused by gas entrapment or contamination. Bian et al. [34] summarize fatigue results in the literature for Ti-6Al-4V produced via the LENS process, noting the inconsistencies between studies. They conclude that process parameters, microstructure, residual stresses, and pores all impact fatigue behavior and thus the process must be optimized for desired fatigue performance. As the primary focus of this thesis involves parts produced via DMLS, a powder bed fusion process, the main focus of this literature review is efforts involving similar powder bed fusion processes.

Svensson [35, 36] studied the fatigue behavior of Ti-6Al-4V produced via EBM. Fatigue testing was performed at $R = 0.1$ and fatigue strengths were compared at 10^7 cycles. Results showed improved fatigue performance from HIP processing to remove porosity. As-built porosity was shown to be 0.19% in the vertical Z build orientation and 0.11% in the X-Y orientation, however porosity was 0% after HIP (See Fig. 3-1 for a depiction of specimen build orientations). Fatigue strength of specimens that had undergone post-build HIP processing was approximately 25% greater than that of the as-fabricated specimens. Additionally, the study results displayed material anisotropy as the as-fabricated specimens built in the X-Y orientation had an 8% greater fatigue strength than those built in the vertical Z orientation, and for HIP-ed specimens this difference was 11%.

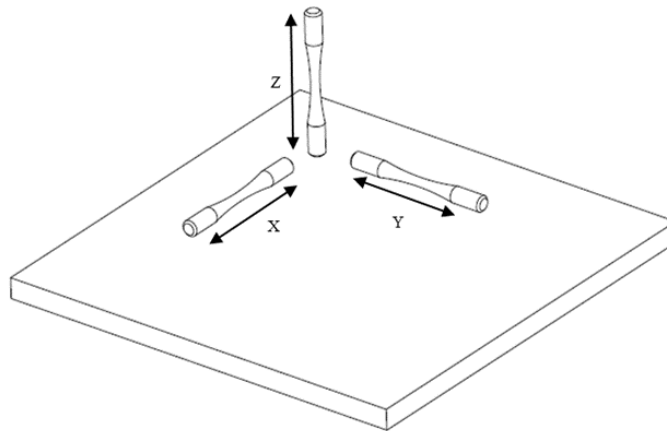


Figure 3-1. Schematic of Referenced Build Orientations (Build Direction is Normal to Platform)

Leuders et al. [37] also evaluated high cycle fatigue behavior of Ti-6Al-4V produced via SLM, primarily focusing on the influence of post-build heat treatments. All specimens tested were built in the vertical Z orientation, and all

were machined to the final geometry. Heat treatment of specimens resulted in 3-10 times greater lives than those of the un-treated specimens (27,000 cycles untreated and up to 290,000 cycles treated), for a given stress amplitude and depending on treatment temperature. Specimens that were HIP-ed did not fail after accumulating 2×10^6 cycles at the same stress level, at which point they were stopped. It was concluded that the presence of pores resulting from the SLM process had a significant effect on crack initiation and fatigue life, far greater than the effect of microstructure. Therefore, HIP-ing improved lives much more effectively than heat treating. It was also concluded that residual stresses in the material primarily influence crack growth behavior. Reducing both of these factors by HIP-ing resulted in fatigue strength comparable to the wrought material.

Edwards and Ramulu [38] investigated the fatigue behavior of Ti-6Al-4V produced via SLM. This study evaluated the impact of both build orientation and surface quality, similar to the research in this thesis. Their results indicate material anisotropy with respect to fatigue life where, for a given number of cycles, the X build orientation displayed fatigue strength 30% greater than the Y orientation and 60% greater than the vertical Z orientation. The authors discuss how differences in microstructure between the orientations may contribute to this anisotropy, however this does not explain how the X and Y orientations show a large difference in fatigue performance yet identical microstructures. Similar to Leuders et al. [37], they conclude that porosity, and the corresponding stress concentrations it introduces, was likely the major contributor to fatigue

performance and that differences in porosity between build orientations are likely and would lead to anisotropy, supported by their qualitative assessment of voids in microscopic images.

Edwards and Ramulu [38] also found that specimens with a machined surface showed no improvement in fatigue performance over specimens in the as-built condition, which is contradictory to the findings of the work herein. They conclude that machining the specimens brings the internal pores to the surface which act as stress concentration points, negating the benefit of removing the rough surface. Overall, fatigue performance of the SLM material was found to be over 75% lower than that of the wrought material due to the effects of microstructure, residual stresses, porosity, and surface finish.

Edwards et al. [39] similarly examined the fatigue behavior of Ti-6Al-4V, produced via the EBM process, for various surface conditions (as-built, machined, and machined plus shot-penned) and in both vertical and horizontal build orientations. Both the rough as-built surface and internal porosity were found to significantly limit fatigue performance. Little difference was observed in fatigue behavior of machined specimens and as-built specimens, which the authors conclude was a result of internal pores being brought to the surface during machining and acting as crack initiation sites. Furthermore, no significant difference was found in fatigue behavior between different build orientations, albeit with a limited number of data points. Overall, the fatigue strengths of the additive manufactured specimens were approximately 80% less than those of the wrought material.

Chan et al. [40] studied the influence of surface finish on fatigue behavior of additive manufactured Ti-6Al-4V specimens produced via both EBM and DMLS processes. This study found higher surface roughness resulting from the EBM process (maximum Ra of 131.4 μm) than the DMLS process (38.5 μm), which was on the order of the respective process layer heights. Surface roughness was found to be related to partially- or un-melted powder particles and layers not being completely filled. Mean fatigue life of the as-built EBM specimens was approximately half of that of the DMLS specimens, and both were improved by machining the surface. Interestingly, Chan et al. did not observe internal pores in either the EBM or DMLS specimens and found that all fatigue cracks initiated at the surfaces. While the fatigue performance of the additive manufactured specimens remained significantly less than that of rolled material, the as-built DMLS specimens did outperform cast material.

Rafi et al. [41] studied the fatigue behavior of SLM produced Ti-6Al-4V. Specimens were machined to net shape and heat treated and only tested in the vertical Z build orientation. Fatigue behavior was better than that of published data for cast and annealed, which was due to the fine microstructure resulting from the rapid cooling during the SLM process. Examination of fracture surfaces uncovered subsurface crack initiation in all specimens which the authors attributed to internal defects.

Wycisk et al. [42] examined high cycle fatigue behavior of additive manufactured Ti-6Al-4V in both an as-built and polished condition, as well as both vertical and 45° “tilted” orientations. Results showed no significant effect on fatigue

performance from build orientation. However, as built specimens showed an endurance limit approximately 60% lower than that of the polished specimens. Additionally, polished specimens had high scatter as stresses approached the endurance limit. This was attributed to the fact that fatigue cracks initiated at both surface defects and internal defects (such as pores), whereas in the as-built specimens all cracks initiated from the rough surface.

3.3 FATIGUE OF OTHER ADDITIVE MANUFACTURED METALS

Spierings et al. [7] researched the fatigue performance of two stainless steels, 316L and 15-5 PH produced via an SLM process and the DMLS process, respectively. For 316L, specimens were produced in as-fabricated, machined, and polished conditions. Test results showed that surface finish influenced the material endurance limit, however at higher stress levels the fatigue behavior was comparable regardless of surface finish. The authors conclude that the spherical powder particles do not act as sharp stress concentrations in the as-fabricated surface. Additionally, Spierings et al. found that the fatigue performance of these stainless steels was less than, but comparable to, published data for conventionally processed material.

The aforementioned studied by Rafi et al. [41] also included an assessment of the fatigue behavior of SLM produced 15-5 PH stainless steel. Specimens were machined to net shape and heat treated and only tested in the vertical build orientation. Fatigue performance of the specimens was lower than published data (20% lower endurance limit) which the authors attributed to the differences in

surface finish between the machined SLM parts and polished specimens in the published data. All cracking initiated on the surface for these specimens.

Brandl et al. [5] examined the fatigue behavior of additive manufactured AlSi10Mg produced via an SLM process. Specimens were produced in three orientations: horizontal in the build plane, or 0°; vertical or 90°; and tilted at 45° to the build tray. Additionally, specimens were produced with two different build platform temperatures and tested both as-built and machined to net shape. Results show that, for the lower build platform temperature, 0° specimens have greater fatigue resistance than 90°, and 45° specimens perform similarly to 90°. This directional dependence is attributed to defects including pores and un-melted spots, which act as stress concentration features and reduce cross-sectional area for loading, thus having a greater effect in the 90° orientation as they are aligned perpendicular to the load. For the higher build platform temperature, there is little difference between orientations and fatigue life is improved. This effect is attributed to less imperfections and lower residual stresses as a result of the higher build temperatures.

Brandl et al. [5] show that for all conditions tested, the fatigue strengths at 5×10^7 cycles exceed those of as-cast AlSi10Mg from published data. Overall, the study concludes that porosity at the surface or sub-surface is the most important factor influencing fatigue life, and notes that process parameters need to be optimized to eliminate porosity as it was seen in all builds.

3.4 TENSILE BEHAVIOR OF ADDITIVE MANUFACTURED METALS

While the focus of this thesis is fatigue behavior, tensile testing was performed and fracture surfaces evaluated, therefore tensile behavior was also reviewed in the literature. However, as mentioned, the majority of the published research in this area has been related to static tensile properties, resulting in a multitude of studies. Thus, this review only included a small number of studies specifically involving Inconel 718 or DMLS to provide relevant insight.

Baufeld [43] performed tensile testing on Inconel 718 produced by a different process, Shaped Metal Deposition (SMD). However, the study also includes a compilation of results from other efforts on static properties of Inconel 718 produced via different laser and electron beam AM processes. The static properties of the additive manufactured material are found to be greater than those of as-cast Inconel 718. This data will be used for comparison with the tensile results in Chapter 6 of this thesis.

Larosa et al. [44] evaluated the tensile behavior of Ti-6Al-4V produced via DMLS and compared with traditionally processed and annealed material. The DMLS samples displayed comparable yield strength and elastic modulus, a higher ultimate strength, and lower ductility. The DMLS sample densities were found to be 98%, indicating some porosity, with a refined microstructure.

Manfredi et al. [45] performed tensile testing on samples of AlSiMg produced via DMLS in different build orientations. All samples were annealed and shot-peened. Samples were found to have 0.7 – 0.8% porosity. Results showed that

for different build orientations within the horizontal build plane, properties were consistent due to the scanning strategy, while vertically built specimens had slightly reduced properties. Results were compared to properties of as-cast aluminum alloy A360 and both yield and ultimate strengths were found to be higher for the DMLS material. The authors conclude that the rapid cooling rates during the build process result in a very fine microstructure which is responsible for the favorable mechanical properties.

Becker et al. [46] similarly conducted tensile testing on samples of Ti-6Al-4V produced via DMLS but with different post-build treatments. As-built specimens are found to have a higher strength than wrought material, again attributed to fine microstructure, however lower ductility. Post-build HIP and heat treatments tended to increase ductility however decrease ultimate strength, which was anticipated based on increased grain sizes.

As is clear in these few studies, DMLS materials have been shown to compare favorably or even outperform wrought materials with respect to static properties. Frazier [36] summarizes the general trends observed in the literature related to static properties, consistent to what was found herein:

“In summary, when properly processed, the static mechanical properties of AM metallic materials are comparable to conventionally fabricated metallic components. The relatively high cooling rates achieved reduce partitioning and favor reduced grain sizes. However, AM fabricated materials do exhibit microstructural and mechanical property anisotropy with the Z-direction generally being the weakest.”

3.5 SUMMARY

In surveying the literature, it is evident that, with respect to the fatigue behavior of additive manufactured metals, results are inconsistent and highly dependent on a multitude of variables. Some studies found fatigue performance comparable to that of wrought material [30, 31] while others found that fatigue performance is drastically less in AM [32, 38, 39]. Some studies found fatigue crack initiation solely at specimen surface [40] while others found cracks forming solely within the material [41]. An effort was made herein to primarily highlight publications involving powder bed fusion processes, but even within this category the processes vary from the use of a laser with SLM and DMLS to the use of an electron beam with EBM. Additionally, the differences in process parameters make it very difficult to compare results across studies.

A common thread was apparent, however, between all of the studies reviewed related to the major factors influencing the mechanical behavior of additive manufactured materials: microstructure, residual stress, surface roughness, and porosity. The research efforts all show that the powder bed fusion processes tend to result in fine microstructures as a result of the rapid cooling rates [37, 38, 39, 41]. Fine microstructure is found to be responsible for the good monotonic tensile properties of AM metals and also influence crack growth behavior, with fine microstructure slowing crack growth [37]. The rough surface characteristic of AM processes has been shown to significantly impact fatigue life [39, 40], and residual stresses induced by the process have been shown to impact crack growth behavior [37].

However, it is the final factor listed, porosity, which was the most consistent finding in all of the literature reviewed. This is particularly the case in studies where the surface quality is improved by a secondary finishing operation, thus reducing the effect of the rough surface on fatigue. For high cycle fatigue, where fatigue life is dominated by crack initiation, the literature predominantly points to porosity as a major limiting factor due to the stress concentrations created by pores. Additionally, Brandl et al. [5] explains that porosity impacts static properties as well because “The defects reduce the effective load-bearing area...”, and this is especially true when loading is perpendicular to layering.

Leuders et al. [47] found the relative density of as-built SLM samples to be 99.77%, while a post-build HIP resulted in no detectable pores. Becker et al. [46] studied specimens of Ti-6Al-4V produced by the same DMLS process and system (EOSINT M 280) used herein and found mean relative densities of 99.79% for as-built versus 99.94% after HIP. Furthermore, Sanz and Garcia Navas [48] measured porosity in samples of Inconel 718 and other materials produced via DMLS. They found porosity levels to be between 0.02 and 0.28%, much lower than that of older technologies. However, as Leuders et al. [47] explain, despite these seemingly high relative densities, “...the effects of remaining pores in case of cyclic loading can be severe.” Kruth et al. [49] showed that process parameters, such as laser scan speed and scan strategy, can have a significant impact on the amount of porosity present. While SLM processes (such as DMLS) can produce parts with over 99% relative density, optimization of process

parameters can lead to relative densities greater than 99.9% [49], in turn influencing material behavior.

Frazier [36] draws the following conclusion related to dynamic properties of additive manufactured metals, which summarizes many of the findings in this literature survey:

“Dynamic properties of AM produced alloys are dominated by defect structures, viz., micro-porosity, and surface finish. However, properly processed HIPed and finished machined AM alloys can exhibit fatigue properties on parity with those of wrought alloys.”

Overall, the majority of work performed in investigating mechanical behavior of additive manufactured metals has been related to Ti-6Al-4V [6] and primarily focused on static properties [5]. This indicates a need for evaluation of both other alloys, such as Inconel 718, and other behavior, such as fatigue, which is critical for many applications. Furthermore, this literature review provided supplemental data for comparison with results obtained herein.

4 EXPERIMENTAL PROCEDURE AND MATERIALS

4.1 EXPERIMENTAL PROCEDURE

The experimental portion of this research began with an assessment of the surface roughness of representative tensile and fatigue specimens using non-contact surface profilometry. In order to characterize the impact of surface quality on fatigue behavior, it was necessary to have a quantitative measure of material surface roughness.

Next, tensile testing was performed on as-fabricated specimens of Inconel 718 in different build orientations. The purpose of this testing was to determine yield strength of the material to utilize in determining appropriate loading during fatigue testing. Typical tension test data (modulus of elasticity, ultimate strength, and percent elongation) was recorded as well and is presented herein.

Rotating-beam fatigue testing was performed on specimens in multiple build orientations and with different surface conditions (as-fabricated versus machined). Number of cycles to failure was recorded at each of three stress levels, approximately 70%, 80%, and 90% of the material yield strength. This data was then utilized in developing stress-life (S-N) curves for the various conditions.

Finally, fractography was performed by examining fracture surfaces of representative tensile and fatigue specimens using a Scanning Electron Microscope (SEM).

4.2 TEST SPECIMENS

All test specimens for this research effort were provided by Stratasys Direct Manufacturing of Austin, TX. All tensile and fatigue specimens for the testing were fabricated using an EOSINT M 280 System, which is manufactured by the German company EOS GmbH Electro-Optical Systems. Table 4-1 contains the DMLS parameters for the fabrication of all specimens herein.

Table 4-1. DMLS Build Parameters

System	EOSINT M 280
Powder Size	-325 Mesh (< 44 μm diameter)
Layer Thickness	40 μm
Laser Power	285 W
Scan Speed	960 mm/s
Scan or Hatch Spacing	0.10 mm
Volumetric Energy Density	74.2 J/mm ³

The stock powder utilized in the build was Inconel Alloy 718 argon-atomized powder provided by Allegheny Technologies Incorporated (ATI) Powder Metals. The material chemistry of the powder used is provided in Table 4-2, and meets the required chemistry listed in ASTM F3055-14 [50] for additive manufactured Inconel 718.

Table 4-2. Powder Composition

Element	Weight (%)
Cr	17.34
Fe	18.55
Mo	3.06
Al	0.55
Ti	0.98
Co	<0.01
Nb	5.19

Mn	0.16
P	0.004
Si	0.01
Cu	<0.01
C	0.029
S	0.002
O	0.018
B	0.002
Ni	Balance

Specimens were produced in multiple build orientations for testing, as depicted in Fig. 4-1.

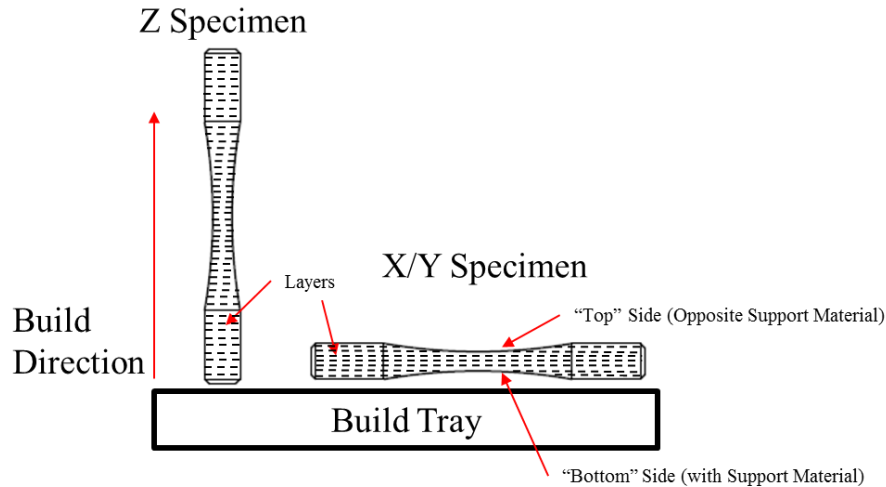


Figure 4-1. Build Orientations

As can be seen, the Z orientation specimens were fabricated in a vertical build direction, while the X and Y orientation samples were fabricated horizontally, lying on edge. This results in build layers across the specimen width in the Z orientation and along the specimen length in the X and Y orientations. Thus the Z orientation specimens contain a greater number of layers. It should also be noted that the X and Y builds were orthogonal in the plane of the build tray (refer to Fig. 3-1 for a three-dimensional view).

As described previously, the DMLS process involves a laser scanning across the part cross-section to fuse the powder material. In this particular build, the scan strategy involved scanning the laser in a pattern of stripes, which rotate in each successive layer (see Fig. 4-2). This rotation results in an even distribution of any differences in solidification. Since both the X and Y orientations experience the same scan pattern, it was anticipated that they would show similar properties.

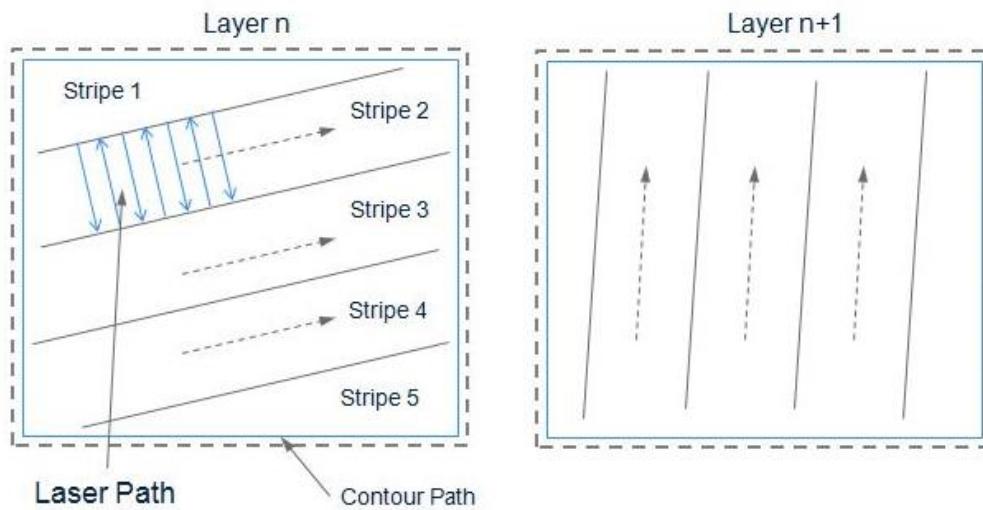


Figure 4-2. DMLS Scan Strategy (Viewing Build Platform from Above)

4.2.1 TENSILE TEST SPECIMENS

For tensile testing, rectangular dog-bone style specimens were fabricated based on the dimensions specified for a sub-size specimen in the ASTM Standard E8/E8M-13a “Standard Test Methods for Tension Testing of Metallic Materials” [51]. A total of four tensile specimens were fabricated, two in the vertical Z orientation and two in the horizontal X orientation (see Fig. 4-1). Figure 4-3 shows the dimensions of the specimen utilized.

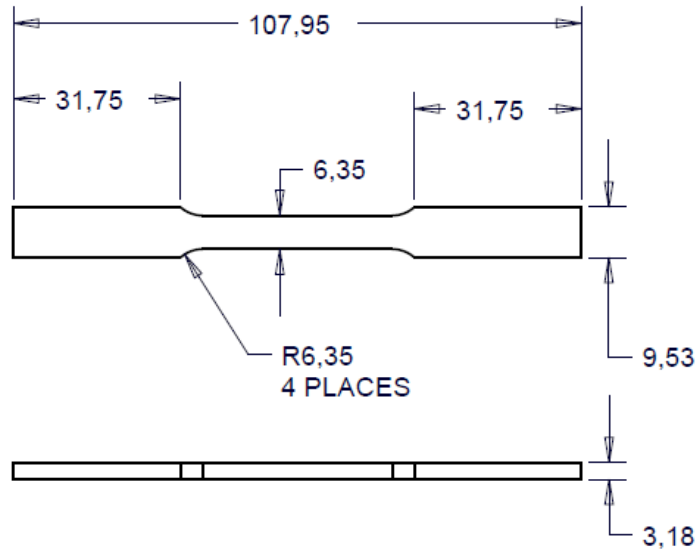


Figure 4-3. Tensile Specimen Dimensions [mm]

Figure 4-4 shows the four tensile specimens produced. Note the presence of darker spots on the left edge of the X orientation specimens which was the surface on the build tray.



Figure 4-4. Tensile Test Specimens

4.2.2 FATIGUE TEST SPECIMENS

For fatigue testing, round hourglass-shaped specimens were produced following the guidelines in ASTM E466-07 [52] as well as dimensions provided in the documentation for the Instron R.R. Moore Rotating Beam Fatigue Testing System [16]. Figure 4-5 shows the fatigue specimen dimensions.

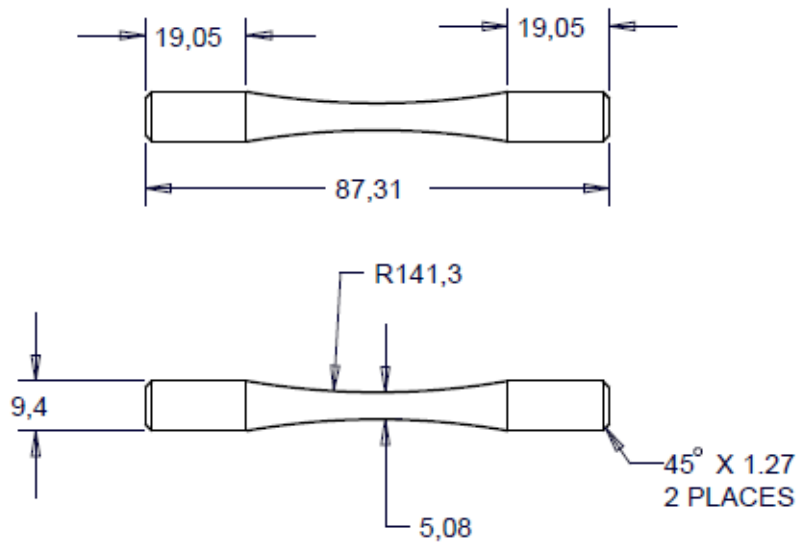


Figure 4-5. Fatigue Specimen Dimensions [mm]

Since the objective of the fatigue testing was to evaluate the impact of both build orientation and surface quality, specimens were fabricated in various orientations and both an as-fabricated condition as well as a machined condition. Fatigue specimens were produced in three orientations, the vertical Z orientation as well as two horizontal orientations, X and Y (See Fig. 4-1).

Eight (8) specimens in the Z orientation, eight (8) in the Y orientation, and seven (7) in the X orientation were machined to final shape for testing. As such, these specimens were produced via the DMLS process with additional stock material

and subsequently turned down to the final shape of Fig. 4-5 on a lathe, thus with surface quality characteristic of the machining process. An additional nine (9) Z specimens, three (3) Y specimens, and three (3) X specimens were fabricated to the final shape using the EOSINT M 280 to be tested with the surface quality resulting from the DMLS process.

Figures 4-6 and 4-7 show the differences between the X and Z orientation specimens. Layering of the X orientation specimen is visible in Fig. 4-6, showing layers parallel to the specimen axis. On the other hand, in Fig. 4-7 the layering of the Z orientation specimen can be seen with layers perpendicular to the specimen axis.

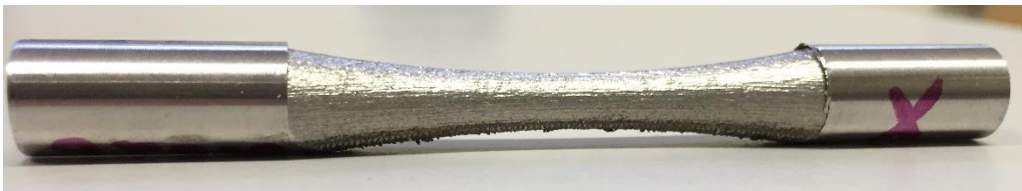


Figure 4-6. X Orientation As-Fabricated Specimen



Figure 4-7. Z Orientation As-Fabricated Specimen

One observation regarding the specimens was the concentricity of the parts. The X and Y orientations, particularly for the fatigue specimens, showed visible

bowing or warping, likely a result of the thermal gradients present during the build. In comparison, the vertical Z specimens had better alignment. It was necessary to correct this misalignment on the as-fabricated X and Y parts due to excessive vibration during testing as will be discussed in Chapter 7. The solution was to machine the ends of these specimens (as can be seen in Fig. 4-6) which improved concentricity sufficiently to reduce chatter during the tests.

Furthermore, the use of support material was necessary to provide structure during the build. For the vertical Z builds of both the tensile and fatigue specimens, the DMLS process did not require support material. For the slight taper of this part, the excess powder in the build chamber provided sufficient support in the vertical orientation. However, for the X and Y builds of both specimens, support material was necessary under the reduced sections to prevent collapse. This support material was removed via a grinding process after the build which, as will be discussed in the following section, resulted in a rough surface. This surface is visible on the underside of the specimen in Fig 4-8.

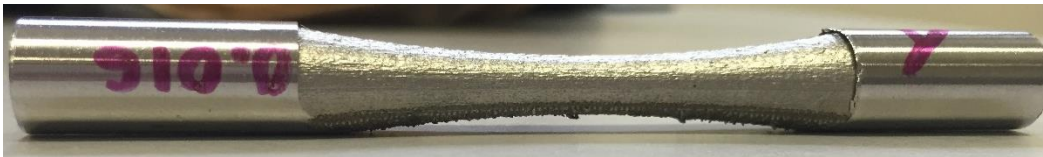


Figure 4-8. Horizontal Y Specimen Rough Underside

As far as number of samples tested, ASTM E739-10 [53] provides guidance on sample sizes for S-N curve development testing. This standard recommends a minimum of 6-12 specimens for research and development testing, which was met

for each condition, assuming the X and Y as-fabricated data is lumped together. Additionally, a percent replication is recommended, which is calculated from the number of samples tested and the number of stress levels, with 33-50% replication recommended for research and development testing of specimens. For three samples at each of three stress levels (achieved in the as-fabricated Z orientation), a percent replication of 67% is achieved. For two samples at each of three stress levels, which was the minimum in the other orientations, a percent replication of 50% is achieved. Thus the number of samples tested was sufficient to meet the ASTM E739-10 criteria.

5 SURFACE CHARACTERIZATION

5.1 PROCEDURE

Surface roughness measurements were performed prior to testing on the four rectangular, dog-bone style tensile specimens as well as on six round fatigue specimens: three as-fabricated and three machined. Evaluation of surface quality was performed at the Tufts University Micro and Nano Fabrication Facility on a Zygo NewView 600S non-contact surface profilometer (see Fig. 5-1).

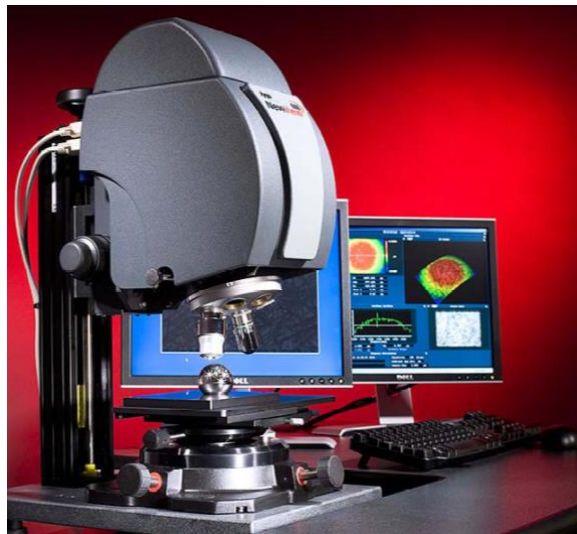


Figure 5-1. Zygo NewView 600S

The NewView 600S uses scanning white light interferometry (SWLI) to provide three-dimensional characterization of surface microstructure and topography. The basic mechanism of SWLI involves detecting interference patterns of light reflected from the surface of the specimen and light reflected from a reference surface. These patterns denote the surface topography and can be measured in three dimensions for a full image and quantification of surface features. [54]

The procedure for performing the surface analysis began with placing the specimen under the NewView microscope such that the light source was directed at the desired measurement location. For the tensile specimens, two measurements were taken in the reduced section of each dog-bone specimen. For the fatigue specimens, two measurements were taken at the center of each specimen, which is where fatigue failure was expected to originate.

Zygo MetroPro software was utilized in controlling the measurements. Scan length was set based on the anticipated roughness for either the as-fabricated or machined surface, and each measurement reported was the average of three scans taken by the equipment for improved accuracy. Beyond these adjustments, the measurement controls were mostly maintained at default settings.

At this point, the scans of the specimens were performed. The software displays a three-dimensional image of the surface and two-dimensional surface profiles among other plots, and the output displays values for maximum peak-to-valley distance, the root-mean-square roughness (RMS), and the average, or arithmetic mean value, roughness (Ra). Figure 5-2 shows an example of the software display.

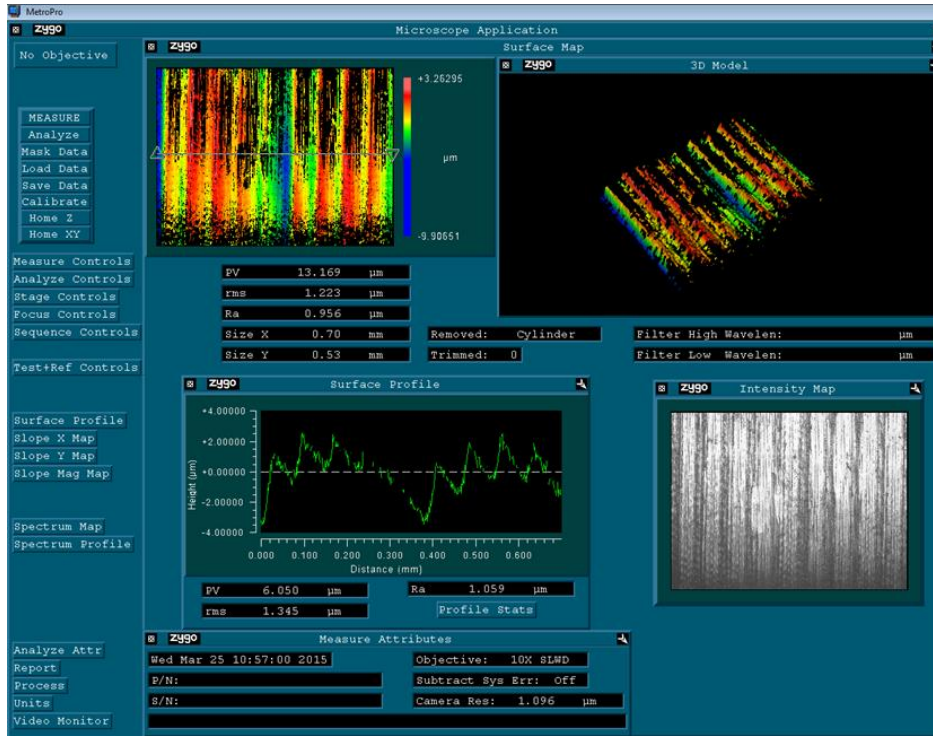


Figure 5-2. Zygo MetroPro Software Display

After completion of the scans, an analysis setting was utilized within the software allowing for subtraction of a surface from the measurements. This was applied to the fatigue specimens by removing a cylindrical surface to account for the curvature of the specimen. While the center section of these specimens is not exactly cylindrical due to the taper, this is a close approximation for the relatively small area viewed under the microscope.

5.2 RESULTS

The data collected during the measurements included a maximum peak-to-valley distance, the root-mean-square roughness (RMS), and the average, or arithmetic mean value, roughness (Ra). These values are presented in Table 5-1 for the as-fabricated tensile specimens, Table 5-2 for the as-fabricated fatigue specimens, and Table 5-3 for the machined fatigue specimens.

Table 5-1. As-Fabricated Tensile Specimen Surface Roughness

Build Orientation	Location	Peak-to-Valley (μm)	RMS (μm)	Ra (μm)
X #1	1	92.43	7.97	5.59
	2	92.87	8.11	5.73
X #2	1	90.26	8.99	6.39
	2	96.26	7.73	5.39
Z #1	1	103.97	14.64	9.83
	2	102.97	12.42	7.34
Z #2	1	91.99	10.52	7.71
	2	92.44	8.82	6.62

Table 5-2. As-Fabricated Fatigue Specimen Surface Roughness

Build Orientation	Location	Peak-to-Valley (μm)	RMS (μm)	Ra (μm)
X	1 “Top”	48.03	6.77	5.42
	2 “Bottom”	103.65	21.47	18.18
Y	1 “Top”	62.01	4.79	3.55
	2 “Bottom”	111.27	20.17	16.34
Z	1	63.82	7.82	6.24
	2	48.26	4.11	3.16

Table 5-3. Machined Fatigue Specimen Surface Roughness

Build Orientation	Location	Peak-to-Valley (μm)	RMS (μm)	Ra (μm)
X	1	17.53	1.49	1.25
	2	21.31	1.84	1.48
Y	1	26.39	2.49	1.93
	2	14.39	1.59	1.28
Z	1	6.80	0.86	0.71
	2	13.17	1.22	0.96

For the tensile specimens, location “1” is at the center of the dog-bone reduced section, and location “2” is near the end of the reduced section. For the fatigue specimens, both locations “1” and “2” are at the center of the reduced section, but

180° apart around the circumference. It should be noted that, for the X and Y orientation as-fabricated fatigue specimens, location “2” (referred to as “bottom”) is significantly rougher than the “top” location 1 due to the removal of the support material from the build on this side (see Fig. 4-1 and Fig. 4-8 in Chapter 4). The Z orientation, on the contrary, has consistent surface quality around the specimen as support material was not required during the build.

5.3 DISCUSSION

As can be seen from the results in Tables 5-1 and 5-2, there is some discrepancy between the roughness measurements of the as-fabricated tensile specimens and the as-fabricated fatigue specimens (considering just the “top” side for X and Y orientations). The average Ra of the X tensile specimens is $5.78 \pm 0.43 \mu\text{m}$, while that of the Z tensile specimen is $7.88 \pm 1.38 \mu\text{m}$. Comparing these two mean values using a t-test results in a *p*-value of 0.027 which, assuming a 0.05 criteria, shows that the difference in roughness between orientations is statistically significant. The as-fabricated X and Y fatigue specimens show an average Ra of $4.49 \pm 1.32 \mu\text{m}$, while the two as-fabricated Z specimen measurements average out to $4.70 \pm 2.18 \mu\text{m}$. These show more consistency between orientations (with fewer measurements), and overall the fatigue specimens show a lower roughness than the tensile.

One contributing factor may have been shape. As mentioned, a cylindrical surface was subtracted from the fatigue specimen data. However, the as-fabricated specimen surface is not as reflective as that of the machined, and

therefore the surface features detected by the equipment were relatively sparse. Figure 5-3 compares the 3D image from the Zygo software of one of the as-fabricated specimens to one of the machined specimens.

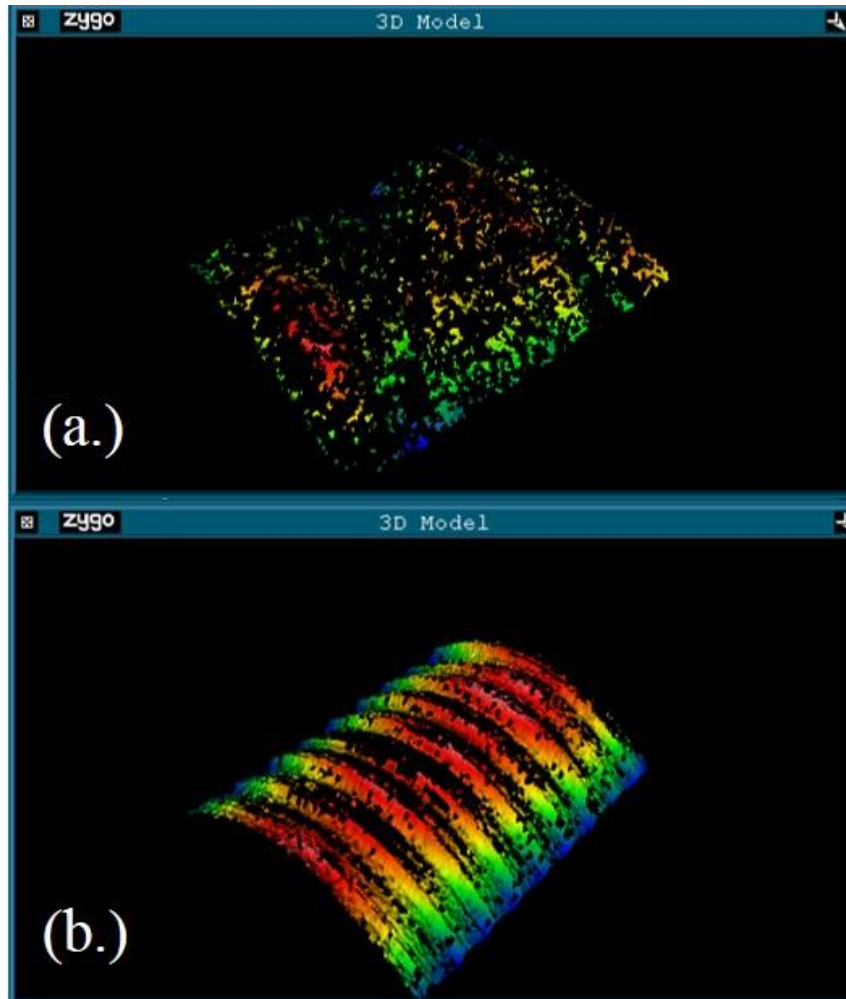


Figure 5-3. Surface Topography of (a.) As-Fabricated and (b.) Machined Specimens

Without being able to capture the entire surface due to lower reflectivity, it is likely that the software is unable to accurately detect the orientation of the underlying cylindrical shape. Therefore, this subtraction may have been slightly inaccurate. It is clear in Fig. 5-3(b.) that the cylindrical form was visible for the machined specimen but not for the as-fabricated. Also, the lack of reflectivity

may have simply caused the equipment not to capture the entirety of the surface profile, as evident in the imaging, therefore resulting in slightly inaccurate results. Since the tensile specimens are planar and may not have introduced the same issues as the round specimens, these numbers were considered more accurate. Thus, the assessment of the as-fabricated specimens shows that the vertical build orientation results in a rougher surface than that of the horizontal orientation.

As for the machined specimens, results were far more consistent, which was expected due to the increased reflectivity of the surface. The X and Y orientation machined specimens had an average Ra value of $1.48 \pm 0.31 \mu\text{m}$, while the Z orientation had an average Ra slightly less, at $0.84 \pm 0.17 \mu\text{m}$. Comparison of these means via a t-test yields a *p*-value of 0.058, slightly greater than 0.05 but close enough to indicate a somewhat significant difference. This trend is consistent with expectations as the X and Y specimens had a slight deformation and lack of concentricity. In contrast, due to the vertical build direction, the Z orientation specimens showed much better alignment. This led to more chatter from the X and Y orientations during rotation on the lathe, and hence a slightly rougher resulting surface quality.

According to Machinery's Handbook [55], average roughness values, Ra, of 0.8 to $1.6 \mu\text{m}$ fall in the typical range for milling and turning. Ra values in the range of 4 to $8 \mu\text{m}$ for the as-fabricated specimens fall in the typical range of forging processes and possibly the lower end of investment casting processes, while the rougher underside of the X and Y specimens (Ra approximately 16 to $18 \mu\text{m}$) are representative of typical sand cast surfaces. These correlations were utilized in

determining empirical surface correction factors for fatigue life predictions, some of which relate typical processes to the correction factor, as discussed in Chapter 7.

The surface roughness data obtained here was also compared to published data found during the literature survey detailed in Chapter 3 of this thesis. Spierings et al. [7] found the average surface roughness of stainless steel produced via a different SLM process to be 10.0 μm as-fabricated, which agrees well with the values of 4 to 8 μm found herein. Edwards and Ramulu [38] reported average surface roughness for yet a different SLM process, which showed higher values on the order of 30 μm . However, their study did find that vertically built specimens had higher surface roughness values than those built horizontally, which is consistent with the findings herein. Chan et al. [40] also report higher surface roughness values for DMLS specimens (built on an EOSINT M 270), listing an Ra value of 38.5 μm .

As Frazier [36] notes, surface roughness is impacted by not only by build direction but also process parameters and equipment, so it is expected that the exact value of the surface finish will vary between these different studies. However, in the most relevant study for comparison, Scott-Emuakpor et al. [30] reported average surface roughness of as-fabricated Inconel 718, produced via DMLS on the same system as herein (EOSINT M 280), to be between 5.08 and 12.7 μm , in close agreement with the values of 4 to 8 μm found herein.

6 TENSILE TESTING

6.1 PROCEDURE

Tensile testing was performed in accordance with the guidelines in ASTM E8/E8M-13a [51] at the Tufts University Materials Testing Laboratory. An Instron Series 5800R Load Frame with a 100 kN [22,500 lbf] load cell was used for testing, as shown in Fig. 6-1.



Figure 6-1. Instron 5800R Load Frame

A preliminary calculation of the load necessary to break the specimen was performed, using ultimate strength data provided on the EOS website [56], and the specimen dimensions. Equation (12) below shows this calculation:

$$P=A*\sigma= (6.35 \text{ mm})*(3.18 \text{ mm})*(1110 \text{ MPa}) = \mathbf{22,414 \text{ N}} \quad (12)$$

The required load of 22.4 kN falls well under the 100 kN limit of the Instron load cell with sufficient margin.

Testing was performed on the two X orientation and two Z orientation tensile specimens described in Chapter 4.2.1 of this thesis. Prior to testing the Inconel specimens, an Aluminum 6061 specimen (built to the same dog-bone configuration) was tested as a reference and to ensure all parameters were properly set.

The test process began by inserting wedge grips into the Instron load frame, jogging into position based on the specimen size, and tightening the grips on the end sections of the specimens. Next, an extensometer was attached to the reduced section of the specimen in order to record accurate strain measurements. The extensometer used was an Instron 2630-104 clip-on extensometer, which is a 12.7 mm [0.5 in] gage length static axial extensometer. Figure 6-2 shows the extensometer attached to a specimen secured within the Instron.



Figure 6-2. Loaded Tensile Specimen with Extensometer

The extensometer was removed after yielding and prior to specimen necking to prevent damage to the gage. Strain values beyond this removal were calculated using a correction based on the final recorded strain.

Testing was controlled via the Instron Bluehill software package. The software was set up for the appropriate tension test method. Specimen dimensions, test rate, extensometer removal criteria, and output data were specified. Testing rate was determined following the recommendations in ASTM E8/E8M-13a for the control method of determining yield properties. A crosshead extension rate of 0.51 mm/minute [0.02 inches/minute] was utilized. Extensometer removal criteria was set to a strain value of 0.5 mm/mm, beyond specimen yield.

The load cell and extensometer were calibrated prior to each session of testing, and prior to each individual test these were balanced and the extension length was

set to zero for the loaded specimen. Data output during the test included time, extension, load, and strain % (based on extensometer readings).

6.2 CALCULATION OF PARAMETERS

The raw tensile test data was analyzed to determine relevant properties such as ultimate tensile strength, 0.2% yield strength, modulus of elasticity, and percent elongation. Additionally, engineering stress versus strain curves were developed by analysis of the raw data. This section details how these calculations were made, with specific results included in Section 6.3.

In order to obtain the ultimate tensile strength, the raw load versus extension data was first plotted, and the maximum load recorded was divided by the specimen cross-sectional area (in the reduced section). The other parameters required the development of a stress versus strain curve.

In order to obtain the engineering stress values, each load recorded in the raw data was divided by the minimum cross sectional area in the reduced section. Since the area reduction due to necking was not accounted for, the value calculated is engineering stress. Strain values were taken directly from the extensometer up until the point it was removed. In order to plot a complete engineering stress versus strain curve, through failure, it was necessary to determine the strain values beyond this point. Equation (13) was applied to calculate corrected strain values based on the final extensometer reading:

$$\varepsilon = \frac{(D - D_P) * \left(\frac{L_e}{L_0}\right) + (\varepsilon_P * L_e)}{L_e} \quad (13)$$

In Eqn. (13), D is the crosshead extension reading (for all points after removal of the extensometer), D_P is the crosshead extension reading at the last point for which the extensometer was attached (Point P), ϵ_P is the strain at point P , L_e is the distance between extensometer “knife edges” or the extensometer gage length of 12.7 mm [0.5 in], and L_o is the gage length of the tensile specimen, or 25.4 mm [1 in] in this case. Engineering stress versus strain curves were then plotted for each specimen.

Next, modulus of elasticity was found by determining the slope in the elastic region of the stress versus strain plots. A linear trend-line was fit to the data using regression analysis, and the slope of this line was taken as the modulus value.

The trend-line was fit in the visibly linear portion of the engineering stress versus strain plots. Figure 6-3 below shows the trend-line created and the corresponding equation for the X1 specimen.

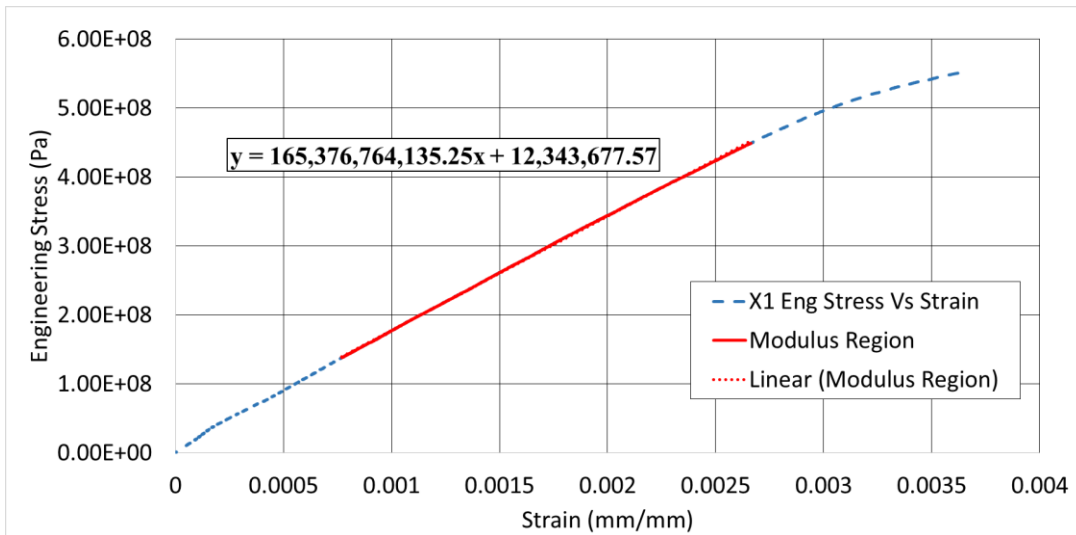


Figure 6-3. Determination of Modulus of Elasticity

In order to determine 0.2% yield strength, a line was plotted with slope equal to the elastic modulus determined for the specimen and with a 0.2% strain offset. The intersection of this line with the engineering stress vs. strain plot was taken to be the yield strength. Figure 6-4 shows an example of this plot for the X1 specimen.

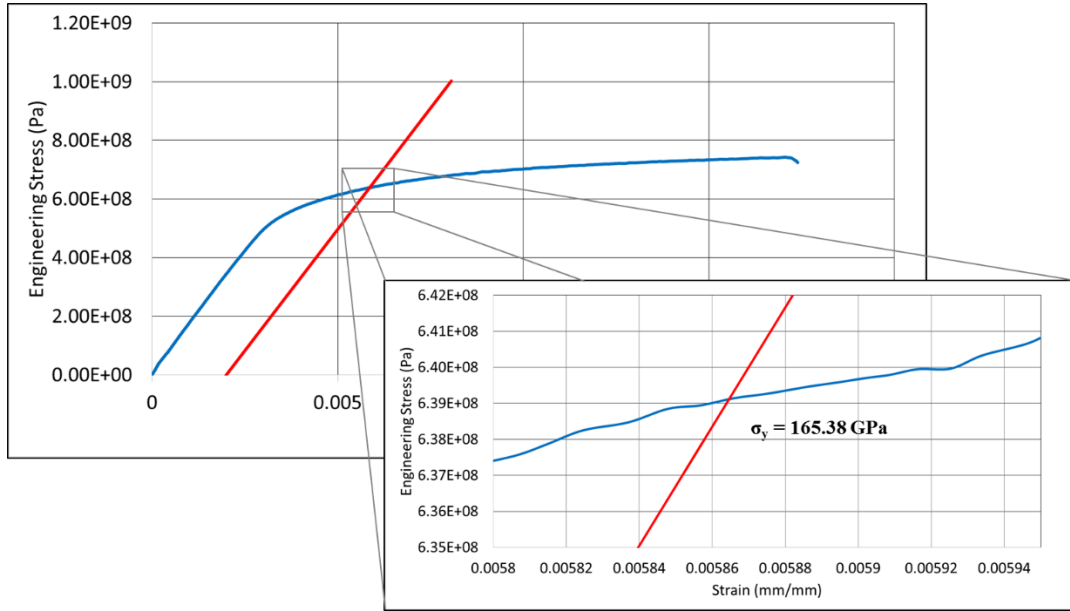


Figure 6-4. Determination of Yield Strength

Finally, percent elongation at failure was determined by reading the strain value from the plot at failure and multiplying by 100 to obtain percent.

6.3 RESULTS

As mentioned in the procedure description, prior to each session of testing an Aluminum 6061 specimen was tensile tested as a control. The testing of these aluminum specimens yielded consistent and expected results for tensile parameters including modulus, yield strength, and tensile strength values. The data for these control specimens is not presented herein.

The raw load versus extension data for all four Inconel 718 specimens is plotted in Fig. 6-5.

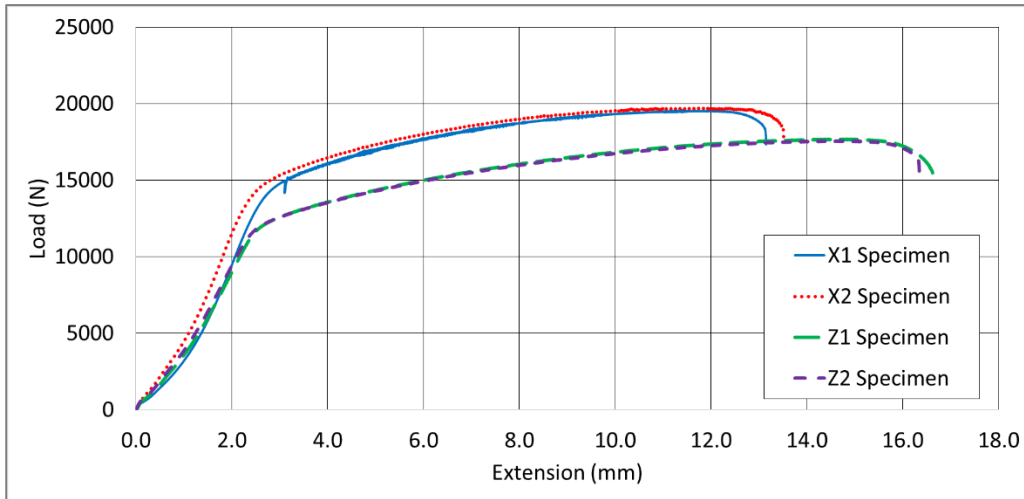


Figure 6-5. Load versus Extension Plot for All Specimens

The first specimen tested was the X1 specimen. One issue was encountered during the testing of this specimen, as the load frame experienced an error and disabled at an approximate strain value of 0.017 mm/mm, or an extension of approximately 3 mm. This appears to have been caused by slippage between the wedge grips and the specimen, likely due to the roughness of the additive manufactured surface. The test was able to be continued and, aside from a minor discontinuity where the error occurred (as can be seen in Fig. 6-5), the results are consistent with those of the other X-orientation specimen. Additionally, this discontinuity did not affect the calculation of any parameters due to the point at which it occurred. A focus was made on securely tightening subsequent specimens to avoid this issue. None of the remaining 3 specimens tested (nor the aluminum control specimens) experienced any issues during performance of the tests.

All four specimens fractured within the reduced section as expected, and all fractures occurred at approximately 45° angles as anticipated for this testing.

Figure 6-6 shows the engineering stress versus strain plots for all four specimens, while Fig. 6-7 has an adjusted x-axis to magnify the elastic region of these curves.

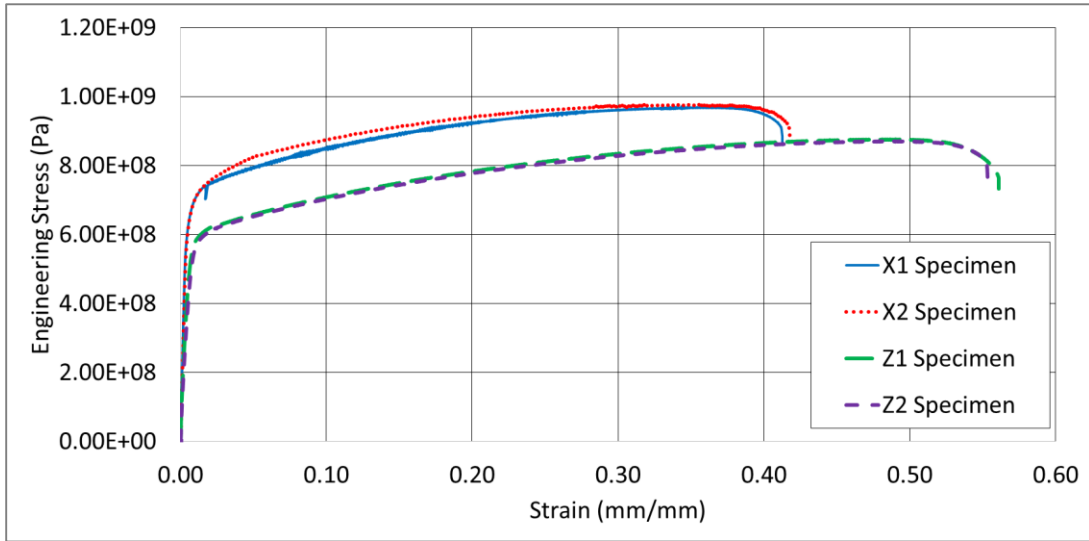


Figure 6-6. Total Engineering Stress versus Strain Curves

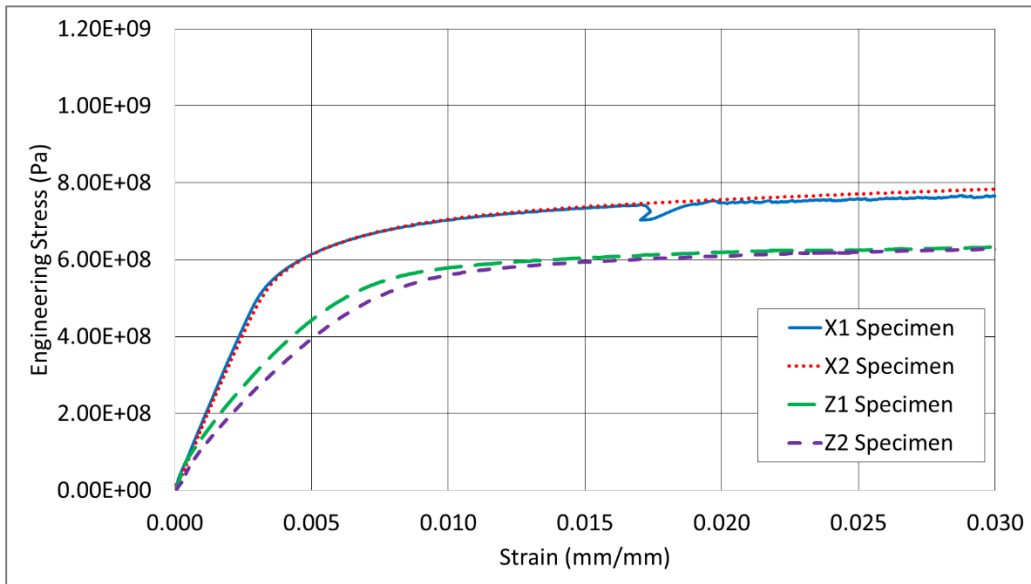


Figure 6-7. Elastic Region of Engineering Stress versus Strain Curves

Table 6-1 below summarizes the values of 0.2% yield strength, modulus of elasticity, ultimate tensile strength, and elongation for each orientation, with averages for the two specimens per orientation.

Table 6-1. Summary of Tensile Testing Results

Build Orientation	0.2% Offset Yield Stress (MPa)	Modulus of Elasticity (GPa)	Tensile Strength (MPa)	Elongation (%) (12.7 mm Gage)
X1	639.1	165.5	971.5	41.3
X2	642.6	160.0	978.4	41.8
Average X	640.9 ± 2.44	162.7 ± 3.90	974.9 ± 4.88	41.6
Z1	573.0	77.2	877.0	56.1
Z2	564.7	66.9	871.5	55.3
Average Z	568.8 ± 5.85	72.1 ± 7.31	874.3 ± 3.90	55.7

6.4 DISCUSSION

As can be seen from Table 6-1, a definitive correlation exists between build orientation and tensile properties. The average 0.2% yield strength and tensile strengths were 11.2% and 10.3% lower, respectively, in the Z orientation than in the X orientation. A more significant effect was seen in elastic modulus, where the modulus in the Z orientation was less than half of that in the X orientation. Furthermore, percent elongation was greater for the Z orientation, indicating increased ductility.

ASTM F3055-14 [50] is a recently published standard covering the additive manufacturing of the nickel alloy UNS N07718, or Inconel 718. This standard provides a table of minimum tensile properties to which the material should conform. It should be noted that these properties were determined with a lower

strain rate than the testing herein, and also involve a stress relief heat treatment. For comparison, the standard specifies a minimum tensile strength in the X/Y orientation of 980 MPa and in the Z orientation of 920 MPa. For the 0.2% offset yield strength, the standard specifies minimums of 635 MPa for the X/Y orientation and 600 MPa for the Z orientation.

The X/Y tensile properties determined herein agree well with the minimums identified in this ASTM standard, and the Z orientation properties determined herein are only approximately 5% less. The stress relief heat treatment included in the ASTM specimens likely accounts for this minor difference, however overall this comparison provides verification of the results herein.

An additional comparison of these tensile results was performed against a data sheet for Inconel 718 available on the EOS website [56]. The data sheet reports ranges of tensile properties for “as-built” material. Both the X and Z yield strengths determined herein were less than the EOS data sheet range, by 12.2% and 2.6%, respectively. The tensile strengths were also both less than the data sheet range, by 3.5% and 6.0% for the X and Z orientations, respectively. Finally, the elastic modulus calculated was within the range for the X orientation, however EOS did not report a value for the Z orientation. It should be reiterated that, while the EOS system was used to build the specimens, the alloy powder was not provided by EOS (as mentioned in Chapter 4.2), possibly accounting for discrepancies.

The study by Baufeld [43] mentioned in Chapter 3 of this thesis contains mechanical properties of additive manufactured Inconel 718 also used for

comparison. Although details on build orientation and process are not provided, Baufeld shows ultimate tensile strengths of 845 – 1000 MPa and 0.2% yield strengths of 552 – 650 MPa for laser beam processes, both in alignment with the results obtained herein. Additionally, Baufeld includes data for as-cast material, listing an ultimate tensile strength of 786 MPa and a 0.2% yield strength of 488 MPa. The additive manufactured material both here and in Baufeld's study outperformed the as-cast material in terms of static properties. This is expected because, as mentioned in the literature review of Chapter 3, the rapid cooling rates in the AM process result in a fine microstructure directly impacting static mechanical properties.

One result that warrants further examination is the significant anisotropy found in elastic modulus with respect to build orientation. Elastic modulus is a function of atomic bond strength [11] and thus an inherent material property. While elastic modulus can be anisotropic within a single grain based on a material's particular crystalline structure, overall in polycrystalline metals modulus is isotropic [11]. As Askeland and Phule [9] note, values of elastic modulus are considered to be independent of microstructure in metals. Thus, microstructural anisotropy resulting from build orientation is likely not the primary cause of the differences in modulus.

One possible explanation is porosity. As Brandl et al. [5] discussed, porosity remaining in the material would reduce the effective area for carrying load. Brandl et al. go on to explain that pores are aligned parallel to layers and thus their impact is evident when loading is perpendicular to the layers. This effect

would explain the results herein, where the modulus in the vertical Z orientation specimens (where tensile load is perpendicular to the layers) was lower. The porosity effect may also be a contributing factor to the anisotropy of the other static properties. Additionally, since the vertical Z build direction has a greater number of layers, there may be a greater probability of pores remaining between layers. Porosity has also been shown to be greater in the vertical build orientation [35, 36] which may have also contributed to the lower Z orientation properties.

However, as the primary focus of the research herein is fatigue behavior, further study into the elastic modulus was not pursued. It should also be reiterated that only two specimens were tested in each orientation, therefore a more significant sample size would be recommended before making definitive conclusions on the properties. Tensile test data was utilized herein primarily to determine the yield strengths in each orientation, which agree well with published data. It is recommended that future efforts be devoted to examining the material modulus in various build orientations.

7 FATIGUE TESTING

7.1 PROCEDURE

High cycle fatigue testing was conducted on an Instron R.R. Moore Rotating Beam Fatigue Testing System at the Tufts University Materials Testing Laboratory. Loads applied during testing were chosen such that induced stresses in the specimens were approximately equal to 70%, 80%, and 90% of material yield strength. As discussed in Chapter 2.1.6, stress levels below yield are applied in this type of test in order to allow for calculation of the induced stresses with elastic relationships. Yield strength measured from the X orientation tensile specimens was utilized in calculating these loads for both the X and Y fatigue specimens. Z tensile test data was utilized for these calculations for the vertical orientation Z fatigue specimens. Table 7-1 shows the applied loading and corresponding stress in the specimen, as well as percentage of yield strength, for each orientation.

Table 7-1. Applied Stresses in Fatigue Specimens

Orientation	Applied Load (lbs)	Stress (MPa)	% of Yield
X/Y	23	579.39	90.4
	19	509.16	79.4
	16	456.49	71.2
Z	19	509.16	89.5
	16	456.49	80.3
	12.5	395.04	69.5

The procedure for performing the tests began with fitting the collets onto the ends of a specimen. Next, the specimen/collet assembly was inserted into the bearing

housings, and the drawbars were inserted and tightened in each housing. Figure 7-1 shows this assembly.

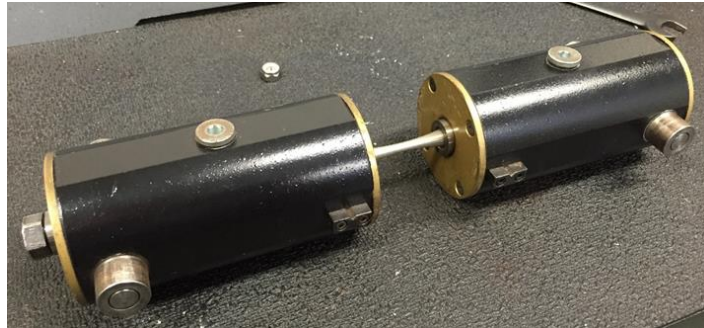


Figure 7-1. Specimen and Bearing Housing Assembly

This assembly was then placed into the apparatus and a set screw was tightened to attach to the motor coupling. The motor was turned on without any load on the specimen in order to ensure there was no excessive chatter with the particular specimen.

Next, with the equipment turned off, the loading harness assembly was hung on the bearings (applying the dead weight to the specimen). The safety cover was closed, and the appropriate weights were added to the loading harness for the particular specimen being tested, per Table 7-1. Figures 7-2 and 7-3 show the R.R. Moore system as well as the loading harness with weights, respectively.

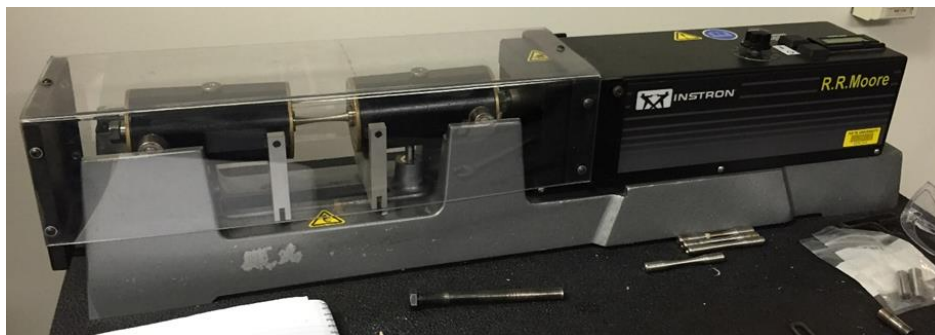


Figure 7-2. Instron R.R. Moore Test Apparatus



Figure 7-3. Loading Harness and Weights

The dial was adjusted to the desired speed, the cycle counter was reset, and the system was turned on. The number of revolutions per minute was measured by reading the value from the counter after one minute and was subsequently recorded for each test. Testing ended automatically upon specimen failure.

Depending on the specimen, test time varied from on the order of minutes to days.

All testing was conducted at room temperature.

Beyond applied weight, the other test parameter that required specification was rotational speed. The test system is capable of rotational speeds up to 10,000 rpm. Through trials of initial test samples, the specimens were found to chatter, sometimes significantly, at lower speeds. To reduce this vibration, testing was conducted at a rotational speed of approximately 6000 rpm (100 Hz), which corresponded to a reading of “50” on the dial (determined via the initial trial runs). As discussed in Chapter 2.1.7, frequency effects on fatigue behavior are considered minimal below 200 Hz [8].

Two minor issues were encountered during testing resulting in stoppage of the test prior to part failure. The first involved the specimens slipping out of the bearing housing and tripping the machine. This slippage was due to variations in both collet sizing and specimen end diameters that led to loosening during testing. This was resolved by measuring all specimen end diameters (as shown in Appendix A) and using the tightest collets on the smaller diameter ends. This only occurred during testing of 2 specimens, which are noted in Appendix A with the raw fatigue data. These two parts were simply reinserted and tightened, and testing was continued without issue.

The second issue encountered involved wear on the motor bushings within the Instron test apparatus. This occurred during 6 tests, and the motor stopped mid-test. This was resolved by removing the machine housing and the motor bushings and cleaning these bushings to improve contact. The particular specimens for which this occurred are noted in Appendix A. Again, testing was continued after the maintenance step. Since the counter stores the number of cycles accumulated until being manually reset, restarting the test simply adds the new cycles to the original total, so nothing is lost as a result of the test stoppages in these instances.

Another issue with the testing related to specimen vibration. As mentioned, the rotational speed chosen resulted in minimal part chatter; however, due to the slight eccentricity of the parts, vibration was not completely eliminated. This was far more pronounced on the horizontally built specimens. Both the as-fabricated and machined Z orientation specimens were more concentric as a result of the vertical build direction, and these specimens produced little to no chatter during

testing. As described in Chapter 4, the X and Y specimens showed visible bowing through the reduced section of the specimen, and therefore even the as-fabricated specimens required machining of the end diameters to improve concentricity for testing. While this reduced chatter, there was still more vibration present than in the Z specimen tests.

In order to understand the degree of this eccentricity, runout was measured at the center diameter of the specimen for a majority of specimens (as-built Z specimens were not measured). These values are included with the raw data in Appendix A. These measurements confirmed the observations, as machined Z specimens all had runouts of 0.010 inches or less, while both the as-fabricated and machined X/Y specimens had runouts ranging from 0.015 to 0.045 inches. An effort was made to utilize the lowest runout values at the lower applied stresses so that chatter would be reduced for the longest tests. Because of the small sample size, a trend was not able to be determined between runout and fatigue life.

7.2 RESULTS

As mentioned, Appendix A contains tables with raw data for each fatigue specimen tested based on condition and orientation. These tables include measurements of the length, center diameter, and both end diameters for each specimen, as well as a measurement of runout at the center of the specimen if available. Also included are the load applied, the life resulting from the test, and the measured rpm and corresponding frequency.

Results of the fatigue testing for the as-fabricated and machined specimens in all three orientations were compiled in an S-N diagram and are presented in Fig. 7-4. It should be noted that one X orientation specimen (with 70% of yield stress applied) did not fail after 10^8 cycles, at which point the test was stopped. This data point is marked with an arrow on the S-N diagram. All other specimens failed at the life shown. Additionally, the S-N diagram includes published fatigue curves for traditionally processed Inconel 718.

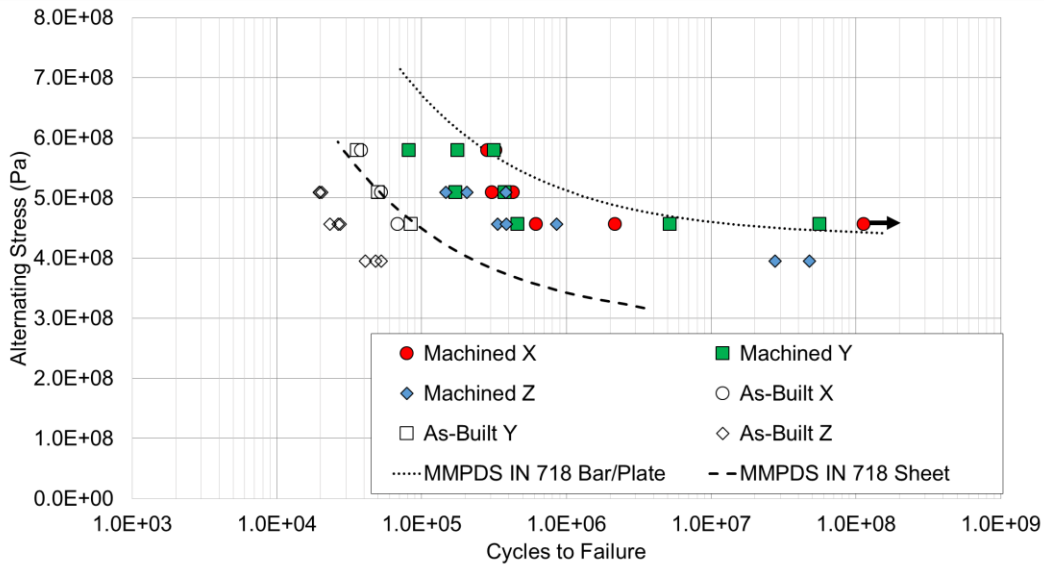


Figure 7-4. S-N Diagram for As-Fabricated and Machined Specimens

7.3 DISCUSSION

As is evident in Fig. 7-4, both surface quality and build orientation had a significant effect on the fatigue behavior of the material. Increase in life was minor, on the order of 2-3X, as stress decreased from 90% to 70% of yield strength for the as-fabricated specimens in a given build orientation. In comparison, the machined specimens showed a far more pronounced increase in life (>100X in some cases) as stress decreased from 90% to 70% of yield strength

for a given build orientation. It is unclear if, at lower stress levels than tested herein, the as-fabricated specimen data would similarly begin to plateau or if it would continue a steep downward trend.

At the highest stress levels tested, machined specimens showed lives on the order of 10 times greater than as-fabricated for a given orientation, while at the lowest stress level this difference was between 100 and 1000 times greater. The large increase in difference at the lower stress level is related to the plateau in the machined data, which will be discussed further below. Nevertheless, it is clear that the as-fabricated surface quality significantly reduced the material fatigue capability across the stress range tested.

Results also indicate a definitive anisotropy in fatigue behavior between the horizontal and vertical build orientations. As anticipated based on the scanning technique in the DMLS process, the horizontal X and Y specimens appear to behave similarly. Due to the small sample sizes, it is difficult to assess if there is a statistically significant difference between the two, but the data appears to be grouped such that there is no discernable difference between the X and Y orientation data.

In the as-fabricated configuration, anisotropy was obvious as the X/Y orientation specimens showed lives approximately 2.5-3 times greater than those in the Z orientation at equivalent stress levels. In the machined configuration, the anisotropy was more evident at lower stress levels. At a stress level of 509.2 MPa, the data for both orientations is grouped closely, with the X/Y orientation

specimens only showing lives approximately 1.3 times greater on average than the Z orientation. However, at the lower stress level of 456.5 MPa, lives are upwards of 25 times greater in the X/Y orientation.

It is clear from the S-N diagram that each orientation in the machined configuration begins to plateau sharply at a stress level of 70% of yield strength. There is also a significant increase in data scatter as stress levels decrease. This is expected as, per Dowling [11], scatter tends to increase with life. Thus, at lower stress levels and longer lives, much greater differences in average lives between orientations are observed.

The plateau and increased scatter at lower stress levels also relate to material endurance limit. As discussed in Chapter 2.1.5, non-ferrous alloys such as Inconel 718 typically do not exhibit a true endurance limit [13], however one can be specified as the fatigue strength at 10^8 cycles [12]. Since testing herein was conducted at three distinct stress levels, the resulting data is not sufficient to accurately predict this limit.

However, due to the plateau in the data, as well as the fact that one of the X orientation specimens did not fail beyond 10^8 cycles, it can be inferred that for the machined specimens in each orientation the endurance limit is at or slightly below 70% of yield. Based on the data in Table 6-1, this means that the X/Y orientation endurance limit is approximately 16% greater than that of the Z orientation.

Thus, for the machined specimens, anisotropy is evident with respect to

endurance limit, while at the highest equivalent stress level tested the data appears to be grouped more closely.

7.3.1 COMPARISON WITH PUBLISHED FATIGUE DATA

The anisotropy observed herein was in agreement with the other published studies discussed in Chapter 3. Edwards and Ramulu [38] found that the horizontal build orientations showed better fatigue performance than vertical (for SLM Ti-6Al-4V), consistent with herein. Svensson [35, 36] found that, for EBM Ti-6Al-4V specimens, fatigue strength was approximately 8% greater in the X/Y orientations than in the Z at 10^7 cycles, which is the same order of magnitude as the estimated 16% difference determined herein for the endurance limit.

Furthermore, Fig. 7-4 includes plots of published fatigue data for traditionally processed Inconel 718. Both curves are from Metallic Materials Properties Development and Standardization (MMPDS) [57]. The two curves are for Inconel 718 bar/plate and sheet specimens, both heat treated, un-notched, under axial loading and $R = -1$. It can be seen that the as-fabricated Z data falls below each of these curves, while the as-fabricated X/Y specimens perform very similarly to the traditionally processed sheet material. The machined specimen data falls between these two curves, with the upper range of the X/Y orientation specimens aligning closely with the Inconel 718 bar data. While this is not an exact comparison due to the heat treatments and different loading condition, results here show promise that the DMLS specimens, with improved surface quality and optimal build orientation for loading, approach the fatigue performance of the traditionally processed material.

Svensson [35, 36] also found that fatigue strength at 10^7 cycles was increased by approximately 25% in each orientation by a post-build HIP process. While HIP was not performed as part of the research herein, and Svensson's study involved a different AM process in EBM, an increase of this order on the machined specimen fatigue data herein would result in fatigue performance greater than that of the traditionally processed bar/plate material. Thus, post-build HIP warrants further investigation as a means to improve performance.

Finally, Scott-Emuakpor et al. [30] plotted fatigue test data on DMLS-produced Inconel 718, with no post-build treatment, that can be compared to the results herein. The condition tested by Scott-Emuakpor et al. equates to the machined Z orientation test specimens herein. At approximately 450 MPa, Scott-Emuakpor et al. show lives ranging from $5e5$ to almost $1e6$ cycles, consistent with the $3.3e5$ to $8.5e5$ cycles herein. Additionally, at approximately 395 MPa, Scott-Emuakpor et al. show lives of $2e6$ and $1e7$ cycles, whereas the results herein at this stress level are $2.8e7$ and $4.8e7$ cycles. Thus, the results herein show good agreement with the only study found in the literature review with fatigue results of DMLS produced Inconel 718.

7.3.2 DETERMINATION OF MATERIAL CONSTANTS

In order to characterize the material fatigue behavior, regression analysis was performed to fit the data with a power relationship. Results are shown in Fig. 7-5

on the S-N diagram for the specimens (X and Y data was grouped for performing this fit).

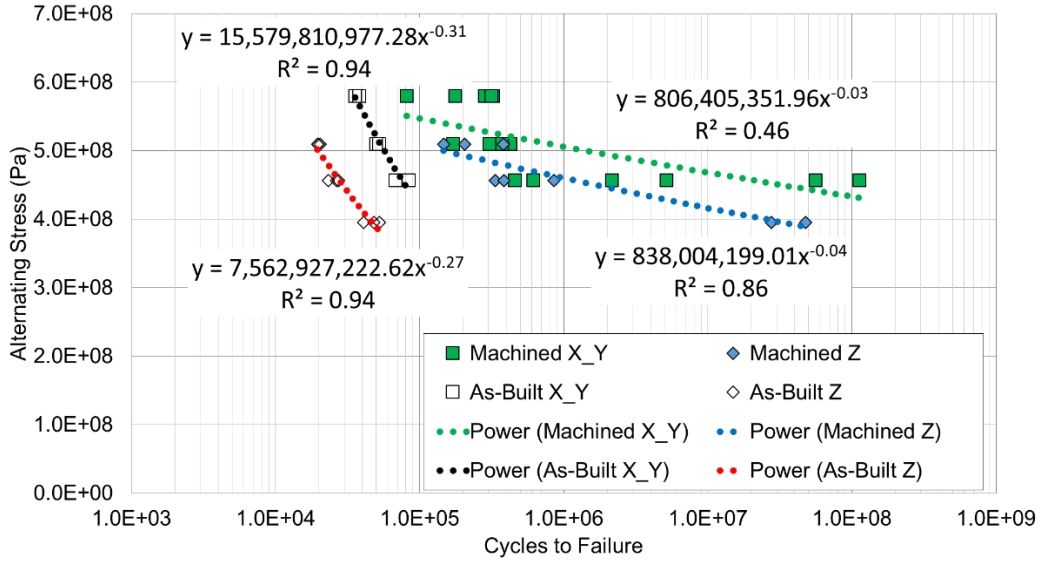


Figure 7-5. S-N Diagram with Curve-Fit Relationships

As described in Chapter 2.1.5 of this thesis, S-N fatigue data can be approximated with the relationship shown in Eqn. (14).

$$\sigma_a = AN_f^B = \sigma'_f(2N_f)^b \tag{14}$$

Based on the relationships plotted in Fig. 7-5, the material constant A and B and the true fracture strength, σ'_f , were determined. Results are summarized in Table 7-2.

Table 7-2. S-N Relationship Constants

Orientation	A	B	True Fracture Strength σ_f (MPa)
X/Y Mach	8.06e8	-0.034	825.6
X/YAs-Fab	15.6e9	-0.31	19314.4
Z Mach	8.38e8	-0.043	863.4
Z As-Fab	7.56e9	-0.27	9119.4

As can be seen, for the machined specimen data, true fracture strengths were 825.6 MPa and 863.4 MPa for the X/Y and Z orientations, respectively. These values are 15% and 1% lower, respectively, than the ultimate tensile strength values presented in Chapter 6 of this thesis. The fracture strengths derived using the as-fabricated data, on the other hand, are on the order 10 times higher than the material ultimate strength, thus very unrealistic.

There are two explanations for these unreasonably high values derived from the as-fabricated data. The first relates to the significant influence of the as-fabricated surface quality on material fatigue behavior resulting in a lower fatigue curve and thus different material constants. The second reason involves the limits of the data acquired in this study. As previously mentioned, the machined specimen data clearly begins to plateau at the lower stress levels tested, while the as-fabricated specimen data follows a linear trend in the stress range tested. It is unclear whether or not at lower stress levels, the as-fabricated specimen data will begin to plateau similar to the machined data, which would impact the curve fits and thus the values listed in Table 7-2.

In order to determine exactly how much surface quality alone influences the values in Table 7-2, testing would need to be extended to lower stress levels for as-fabricated specimens to refine the curve fits. Either way, it is still clear from this assessment that as-fabricated surface quality impacts these material constants.

Within the limits of this study, it is thus evident that the as-fabricated data cannot be interpreted to determine intrinsic material properties. The true fracture strength calculated based on the machined data, on the other hand, aligned well with the average ultimate tensile strength and thus the machined specimen results appear to be more indicative of the actual material capabilities.

Values of A , B and σ_f' have come to be considered material properties [11], thus this effort has contributed a characterization of these properties to the literature for comparison with future research. Additionally, it is clear that, when determining these properties for additive manufactured materials, it is necessary to specify the corresponding surface condition due to its significant influence.

7.3.3 COMPARISON WITH RULE-OF-THUMB CALCULATIONS

As detailed in Chapter 2.1.5 of this thesis, empirical relationships exist for determining S-N curves for steels based upon material monotonic properties, particularly ultimate strength; however, these relationships are not defined for other materials [13]. Despite this fact, the approach for steels was applied herein to compare with the test data and evaluate its validity as a possible design tool for engineers to use with additive manufactured materials.

The assumed empirical relationships include equating the fatigue strength at 1000 cycles to 90% of ultimate strength and equating the material endurance limit (at 10^6 cycles) to 50% of ultimate strength. While 50% is typically assumed for endurance limit, it is known to range from 35% to 60% of ultimate strength for steels [8, 13]. Since the endurance limit for the Inconel 718 specimens tested herein is assumed to be approximately 70% of yield strength, as discussed in the beginning of this chapter, the empirical relationship was adjusted to equate endurance limit to 47% and 45% of ultimate strength for the X/Y and Z orientations, respectively. The power law relationships shown in Eqn. (6) to Eqn. (8) are then used to predict the S-N curve between 10^3 and 10^6 cycles. Using the ultimate strength values determined from the tensile testing herein (summarized in Table 6-1), predicted S-N curves were developed for the Z and X/Y orientations. Figure 7-6 shows an overlay of the fatigue test results and these predicted curves.

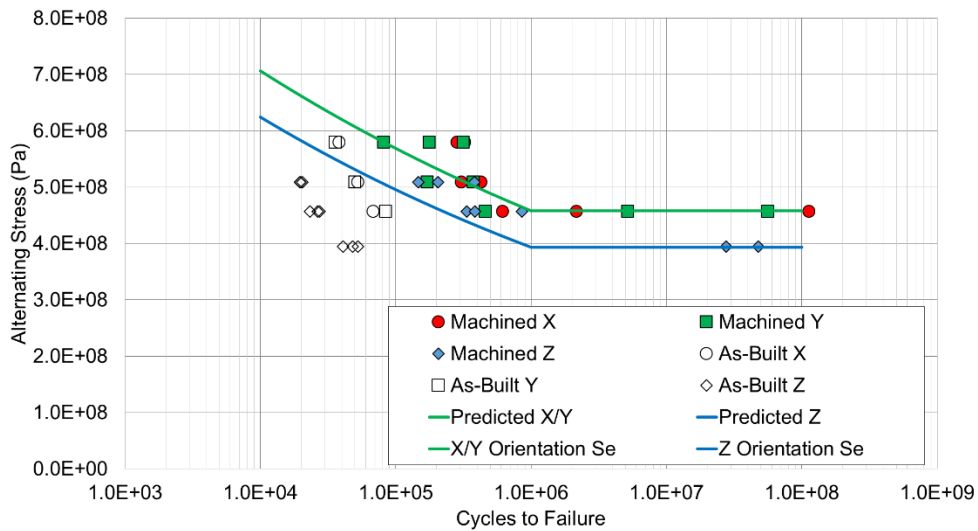


Figure 7-6. Predicted S-N Relationships vs. Test Data

As can be seen, the prediction curves show good visual agreement with the X/Y machined data below 10^6 cycles but underestimate the fatigue strength of the Z

orientation machined data in this range. Since the predictions were calculated using the assumed endurance limit of the machined specimens, it clearly is not applicable to the as-fabricated data, which falls below the curve.

There appears to be promise that these empirical relationships could provide engineers with a conservative estimate of the performance of additive manufactured Inconel 718, which would be a useful tool in the design phase. Since the prediction requires an assumption for endurance limit as a percentage of ultimate strength, this evaluation found that approximately 45% appears appropriate for machined surface, Inconel 718 specimens. Further testing to more precisely determine endurance limits in each orientation, and for each surface quality, could refine these predictions. Based on these results, however, this approach is not recommended as much more than a design tool with this material as it does not appear to provide an accurate enough approximation across the range of lives

7.3.4 COMPARISON WITH SURFACE ROUGHNESS CORRELATION FACTORS

Finally, published modifying factors related to the effects of surface finish on fatigue behavior were evaluated. As mentioned in the surface roughness results, the Ra values for the as-fabricated specimen were equivalent to those of typical forging processes. As discussed in Chapter 2, Juvinall and Marshek [12] present a plot of surface factor versus tensile strength for various finishes, where the surface factor is the reduction in endurance limit from a mirror polished part. Using the tensile strengths obtained in the testing herein, the correlation factors are

approximately 0.72 for a machined surface versus 0.35 for an as-forged surface. This results in a predicted difference between machined and as-fabricated of approximately 2.1 times.

Bannantine et al. [13] similarly shows a plot relating surface factor to ultimate tensile strength based on average surface roughness values. Using the surface roughnesses determined herein, this plot predicts a lower value than that in Juvinal and Marshek, a factor of approximately 1.2 between as-fabricated and machined. As Bannantine et al. [13] note, while these modification factors are meant for endurance limit, they can be applied to fatigue strengths across the S-N curve, however they result in a conservative estimate as these factors tend to have less influence at shorter lives. Both the 2.1 and 1.2 factors were applied to the machined data fatigue strengths and plotted on the S-N diagram with the as-fabricated data in Fig. 7-7.

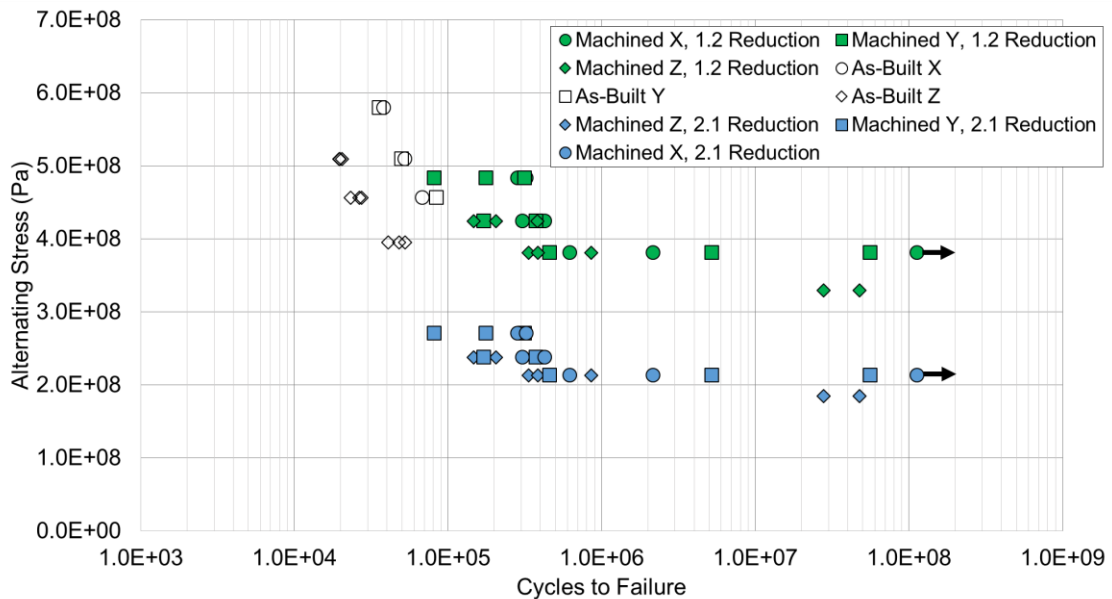


Figure 7-7. Assessment of Surface Modifying Factors

While further testing of the as-fabricated specimens would be necessary to compare to these reduction factors, a rough comparison can be made by assuming the as-fabricated data will follow a similar trend to the machined data and begin to plateau. The 1.2 factor derived from Bannantine et al. appears to over-predict the fatigue behavior of the as-fabricated data, only slightly for the horizontal orientations but more for the vertical orientation. This is expected as, due to the differences in surface roughness between orientations explained in Chapter 5, it was anticipated that different factors would apply to each. On the other hand, the 2.1 factor from Juvinall and Marshek appears to under-predict the as-fabricated results, again with a greater under-prediction of the horizontal data. Therefore, based on the results herein, a surface factor somewhere between these two values (likely closer to the 2.1 value for vertical specimens and closer to the 1.2 factor for horizontal specimens) appears to predict the reduction in fatigue behavior between a machined surface and as-built DMLS surface specimen.

These factors can also be used to predict endurance limits of the as-fabricated specimens. Assuming endurance limit of the machined specimens is approximately 70% of yield strength (as discussed at the beginning of this chapter) and applying the more conservative factor of 2.1 results in predicted endurance limits of 217 MPa and 188 MPa for the X/Y and Z build orientations, respectively, in an as-fabricated state. Similarly, using the factor of 1.2 results in predicted endurance limits of 380 MPa and 329 MPa for the as-fabricated X/Y and Z orientations, respectively.

8 FRACTOGRAPHY

8.1 PROCEDURE

Fracture surfaces of representative tensile and fatigue specimens were examined using a Scanning Electron Microscope (SEM). Imaging was performed on a Phenom Pro desktop SEM, as shown in Fig. 8-1.



Figure 8-1. Phenom Pro Desktop SEM [Photo courtesy of www.phenom-world.com]

The system optical imaging capability was utilized to capture 20X magnification overall images of fracture surface. Higher magnification SEM images of various portions of the fracture surface were then taken.

In order to accommodate the size requirement of the SEM sample holder, it was necessary to cut the specimens to approximately 1 inch lengths. One X and one Z tensile specimen were examined, along with eight fatigue specimens compromising each build orientation and surface condition.

8.2 TENSILE FRACTURE SURFACES

Figure 8-2 shows optical images of the fracture surfaces for the X and Z tensile specimens evaluated.

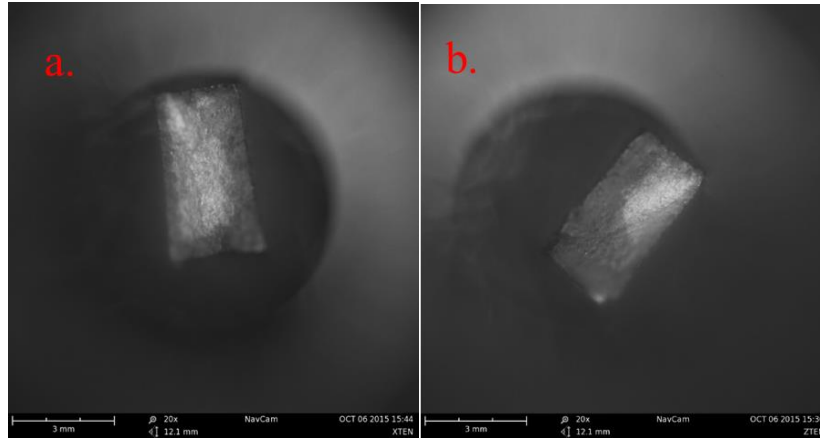


Figure 8-2. Images of (a.) X and (b.) Z Tensile Specimens [20X Magnification]

These images are not completely clear due to the steep height changes in these fracture surfaces. Figure 8-3 below includes photos of the fracture surfaces to better depict these features.

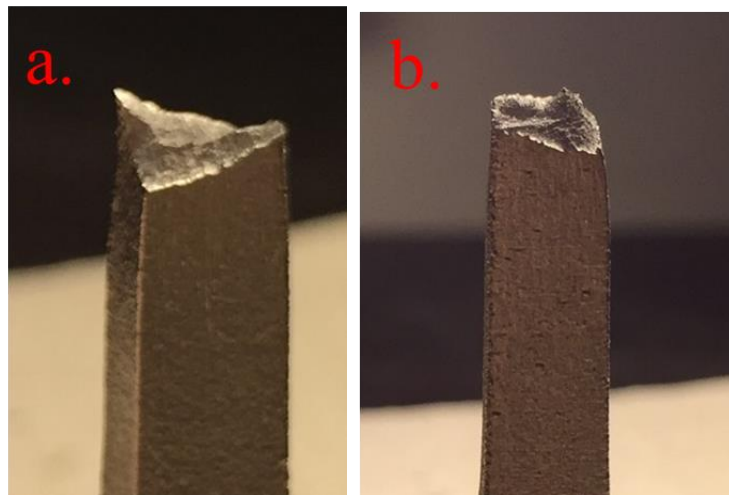


Figure 8-3. Tensile Fracture Surfaces for (a.) X and (b.) Z Orientation Specimens

As can be seen, both exhibit 45° fracture surfaces, consistent with the orientation of highest shear stress in a tensile test, with steep height changes. The X orientation surface appears to shear in two directions, while the Z orientation exhibits a traditional shear surface. Additionally, necking is evident in these sections, characteristic of ductile fracture.

Figure 8-4 shows two magnifications of the fracture surface for the X orientation tensile specimen.

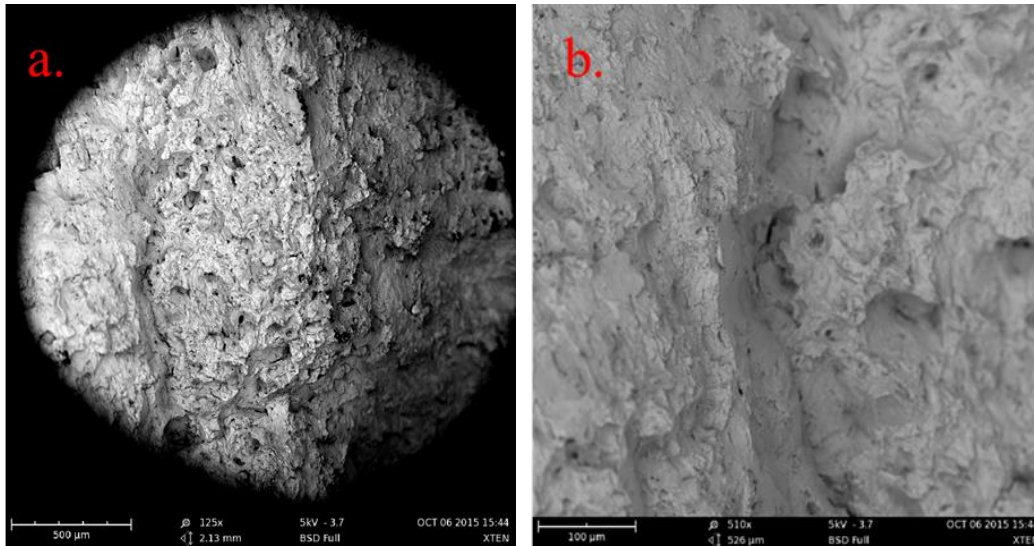


Figure 8-4. X Orientation Tensile Specimen SEM Images at (a.) 125X and (b.) 510X Magnification

These images show evidence of dimples, which indicate microvoid coalescence as the fracture mechanism [9]. This is consistent with tensile fracture behavior for ductile materials.

One significant finding in the SEM imaging of the tensile specimens was the presence of pores. Porosity has been mentioned throughout this thesis as a

significant factor in both fatigue and tensile performance. Figure 8-5 shows three levels of magnification on a pore in the Z orientation specimen.

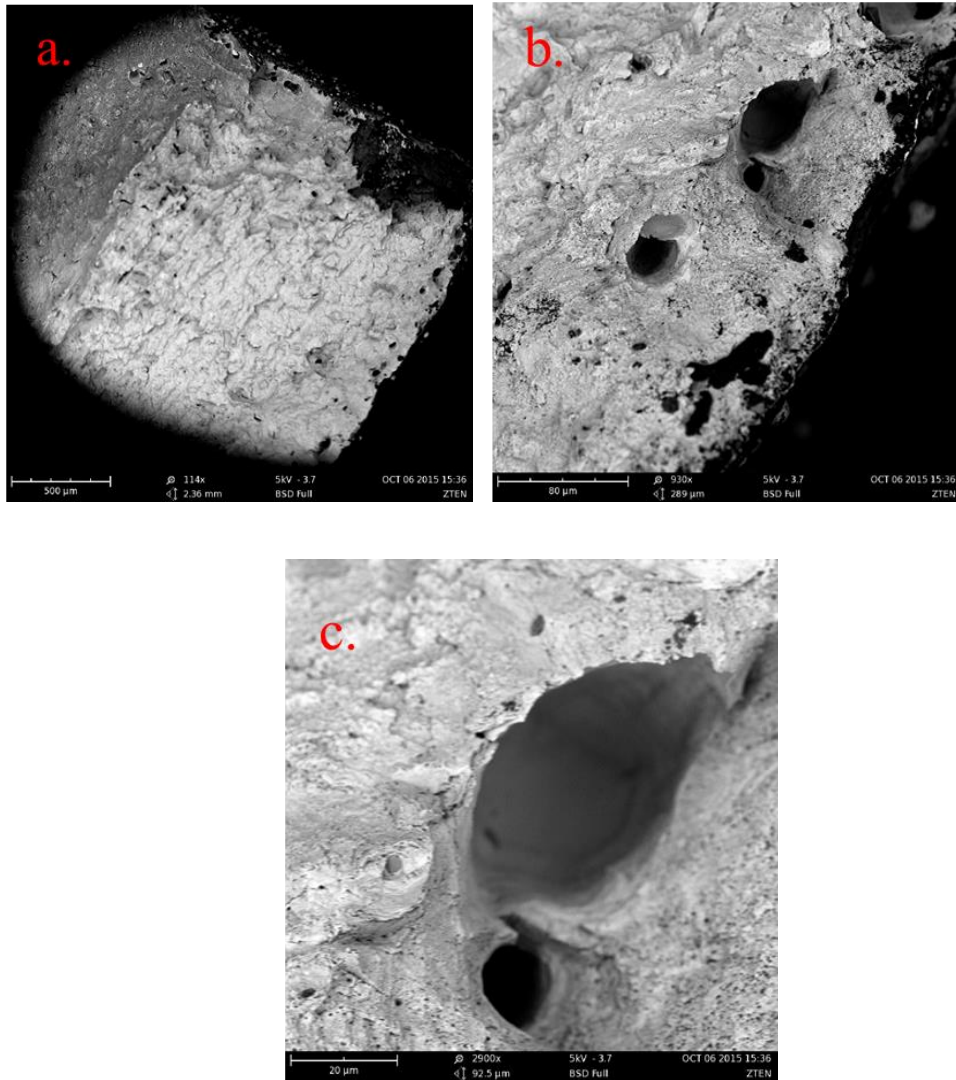


Figure 8-5. Porosity in Z Orientation Tensile Specimen at (a.) 114X, (b.) 930X, and (c.) 2900X Magnification

The pore in Fig. 8-5(c.) is approximately 20 μm across based on the scale in the image. This aligns with the potential size of a powder particle, as the layer thickness in these builds is 40 μm and powder particles of less than 44 μm diameter were used.

8.3 FATIGUE FRACTURE SURFACES

Figure 8-6 contains optical images of four machined fatigue specimens examined using the SEM.

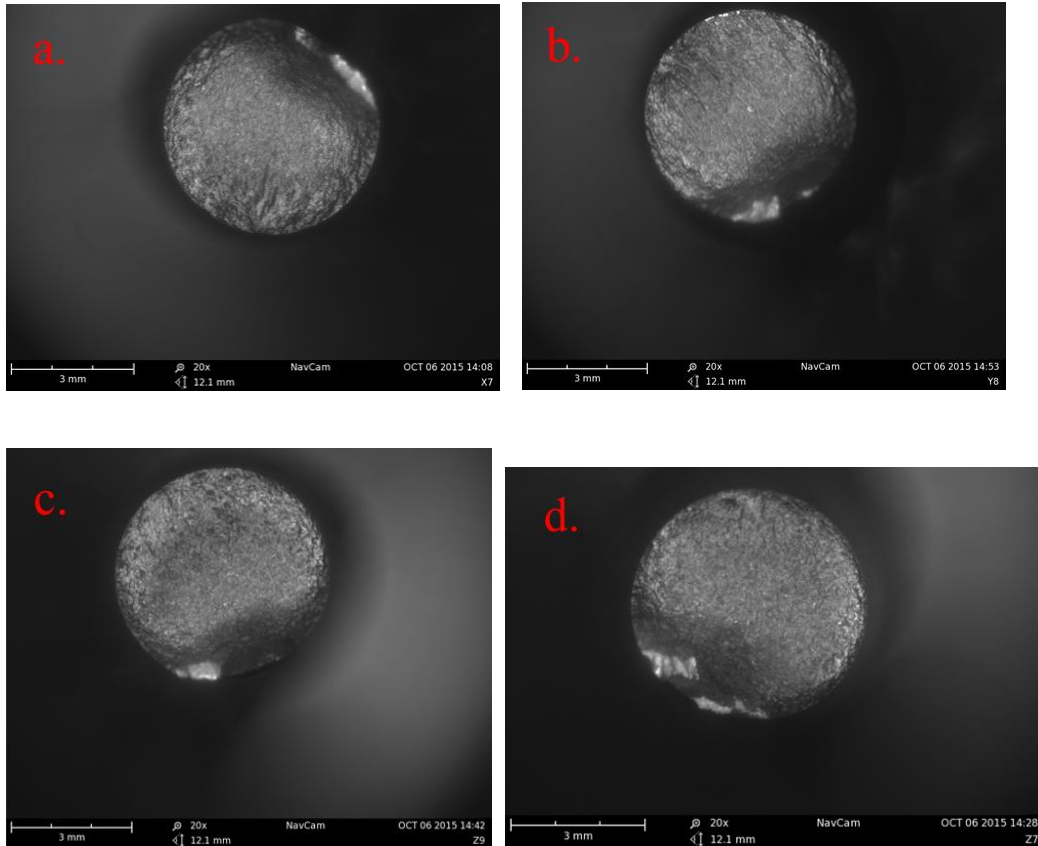


Figure 8-6. Fracture Surfaces of Machined Specimens (a.) X7, (b.) Y8, (c.) Z9, and (d.) Z7 [20X Magnification]

The four specimens shown here are X7, Y8, Z7, and Z9. X7, Y8, and Z9 were all tested at 70% of yield strength and had fatigue lives of 2.2×10^6 , 5.6×10^7 , and 4.8×10^7 cycles, respectively. Z7 was tested at the highest stress level, 90% of yield, with a life of 3.8×10^5 cycles.

The images show evidence of many of the characteristic features of fatigue fracture discussed in Chapter 2.1.2. Beach marks are not present on the

specimens; however, crack initiation sites, smooth crack growth regions, and coarse final fracture regions are visible on the surfaces. Furthermore, although difficult to see in the image, the edge of the specimen in the fracture region contains a shear lip, characteristic of ductile metals such as Inconel 718. Figure 8-7 shows the image of the Y8 fracture surface with regions identified.

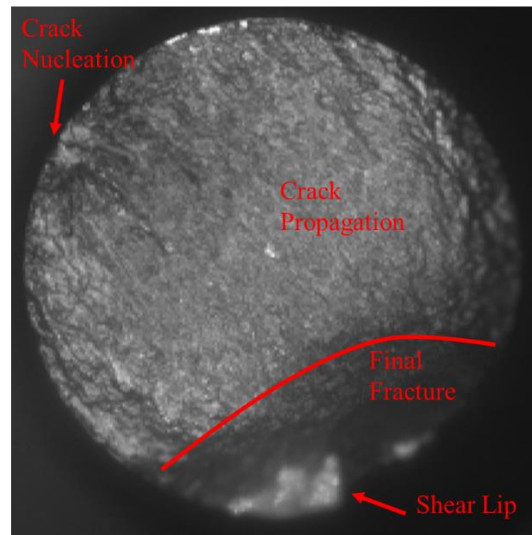


Figure 8-7. Fracture Surface Features [20X] (Machined Y8 Specimen)

Figure 8-8 contains a magnified view of the crack initiation site on the Y8 specimen along with the crack propagation region.

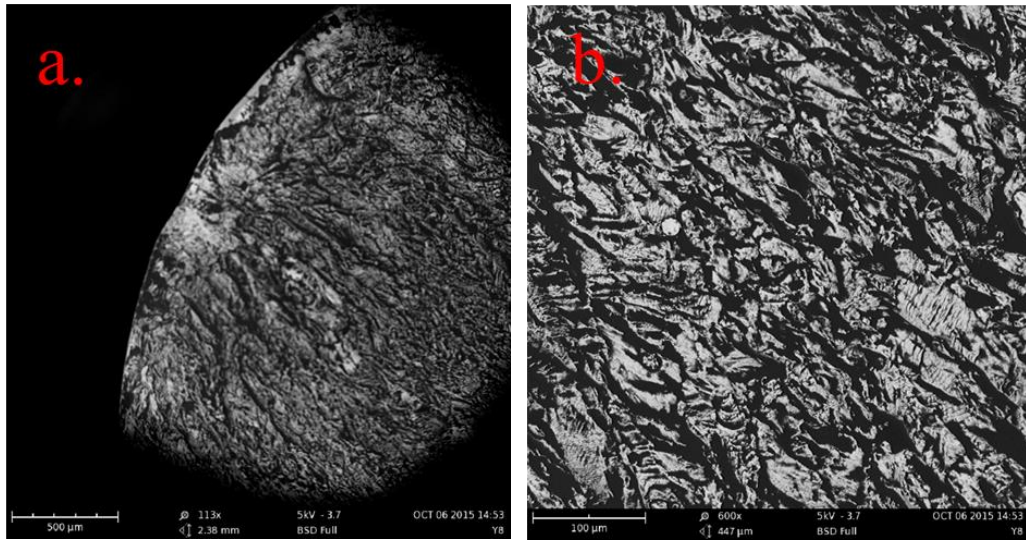


Figure 8-8. SEM Images of (a.) Crack Initiation Site [113X] and (b.) Crack Progression Region [600X] (Machined Y8 Specimen)

The crack initiation site in Fig. 8-8(a.) appears to be a subsurface pore or defect, which is likely a result of the improved surface finish due to machining.

Additionally, in the crack propagation region in Fig. 8-8(b.), fine striation marks are visible indicating location of the crack tip during growth.

Figure 8-9 below shows the area of crack nucleation in the Z9 specimen at two magnifications.

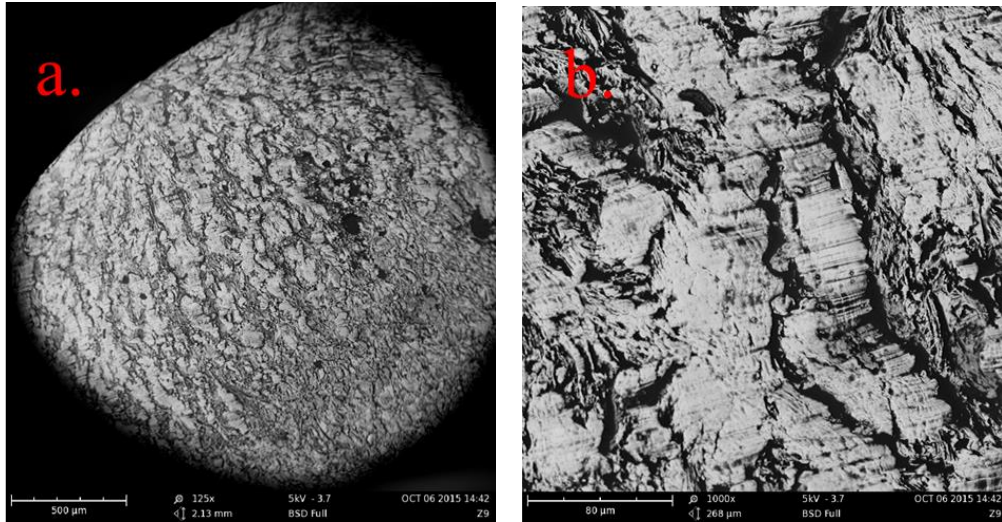


Figure 8-9. SEM Images of (a.) Crack Initiation [125X] and (b.) Crack Progression [1000X] (Machined Z9 Specimen)

At the higher magnification in Fig. 8-9(b.), the crack propagation is clear, again with striation marks visible. Figure 8-10 includes a lower magnification view of the transition region from crack growth to final fracture, as well as a magnified view of the final fracture region, for the same Z9 specimen.

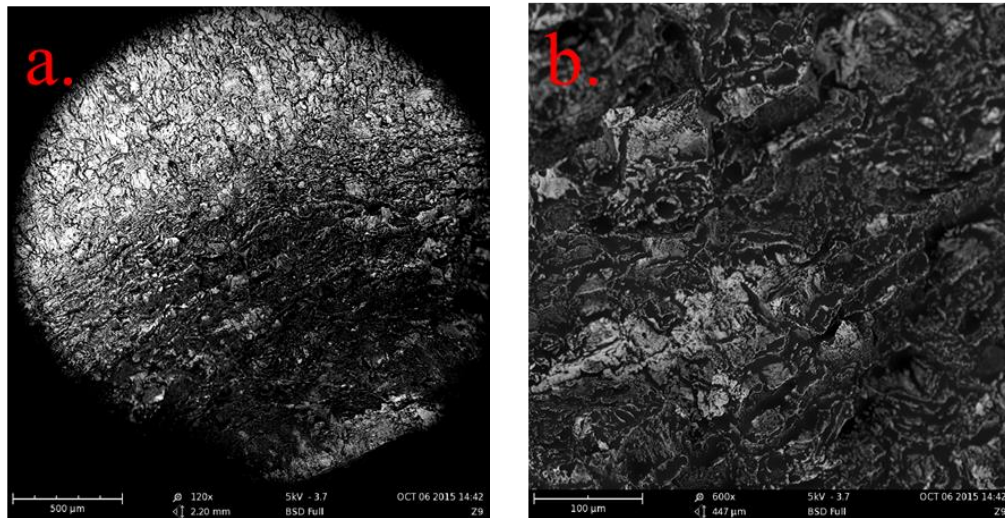


Figure 8-10. SEM Images of (a.) Transition Region [120X] and (b.) Final Fracture Region [600X] (Machined Z9 Specimen)

The coarser final fracture region is evident in Fig. 8-10(b.), with a dimple pattern indicative of ductile fracture.

Despite the fact that the Z7 specimen experienced two orders of magnitude less fatigue cycles than the other specimens, the fracture surface features are very similar. This may be explained by the fact that, despite the differences in total lives, all of the tests conducted were still in the high cycle fatigue range.

Figure 8-11 contains optical images of four as-fabricated fatigue specimens examined.

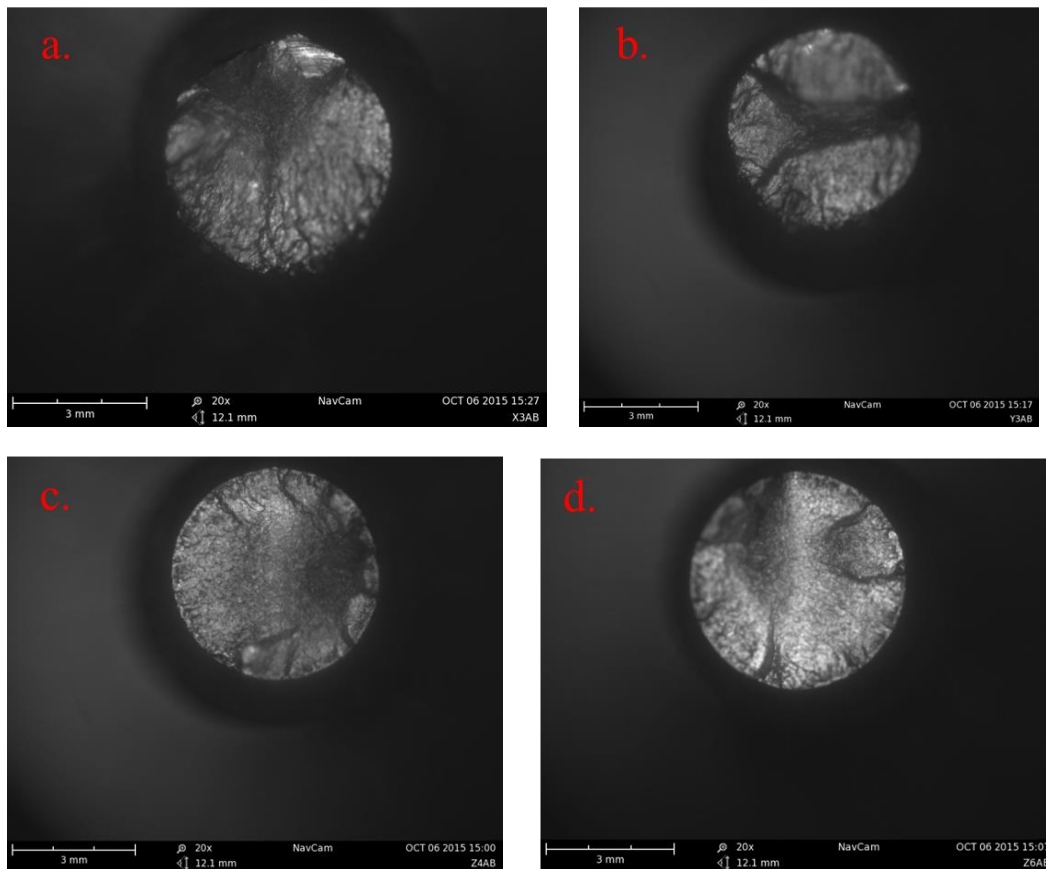


Figure 8-11. Fracture Surfaces of As-Fabricated Specimens (a.) X3, (b.) Y3, (c.) Z4, and (d.) Z6 [20X Magnification]

The four specimens shown here are X3, Y3, Z4, and Z6 as-fabricated. X3, Y3, and Z4 were all tested at 90% of yield strength and had fatigue lives of $3.8e4$, $3.6e4$, and $2.0e4$ cycles, respectively. Z6 was tested at the lowest stress level, 70% of yield, with a life of $5.2e4$ cycles.

These as-fabricated fracture surfaces are clearly different from those of the machined specimens in Fig. 8-6. Most noticeably, cracks appear to initiate from multiple sites around the specimen. This is consistent with the literature, as Edwards et al. [39] similarly found multisite surface crack nucleation in as-built specimens and no clear crack propagation region.

Each of the specimens in Fig. 8-11 displays a different pattern based on the crack sites, with final fracture likely occurring in the darker regions. Furthermore, these surfaces are jagged unlike the machined specimens, indicating that cracks are potentially forming on multiple build layers and coalescing.

Fig. 8-12 contains higher magnification views of the Z4 as-fabricated specimen.

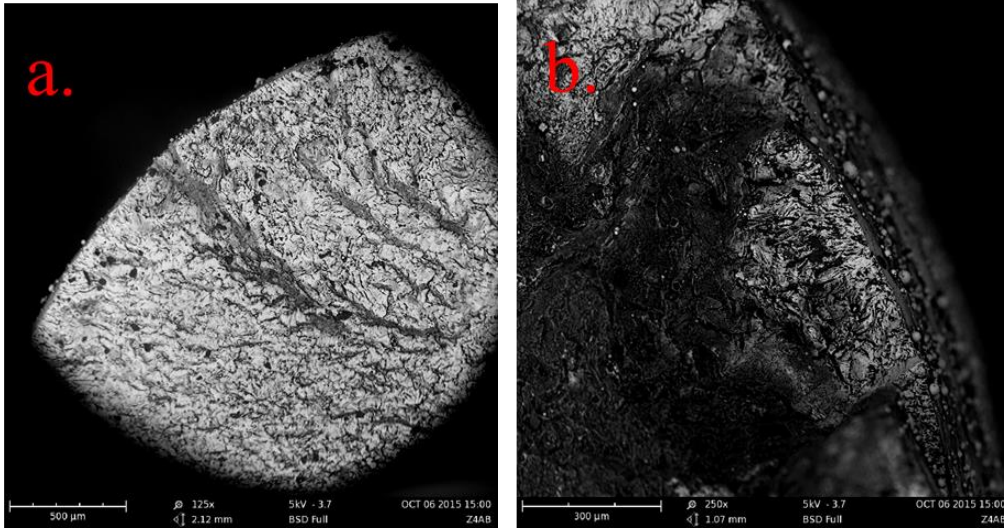


Figure 8-12. SEM Images of (a.) Crack [125X] and (b.) Final Fracture [250X] (As-Fabricated Z4 Specimen)

The dark area in Fig. 8-12(b.) appears to be the region of final fracture, and it contains dimples again indicating ductile fracture, while Fig. 8-12(a.) appears to show cracks initiating from the surface.

Figure 8-13 shows a magnified image of the as-fabricated X3 specimen at the lower surface.

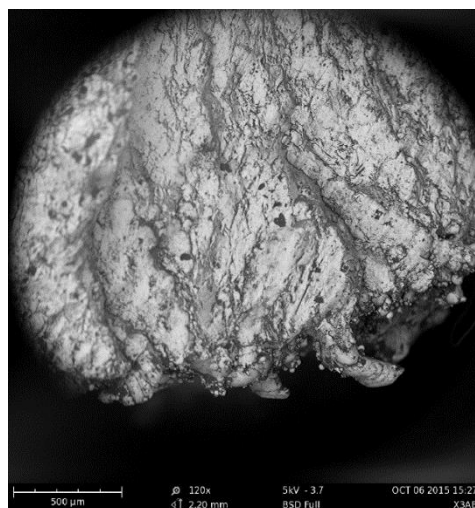


Figure 8-13. SEM Image of Crack Propagation [120X] (As-Fabricated X3 Specimen)

This is the very rough underside of the specimen, as explained in Chapter 4, and the surface roughness characteristics are visible in this image. Additionally, the crack progression is evident in this region.

Figure 8-14 includes two magnifications of the edge of the Y3 as-fabricated specimen surface, where it appears a crack initiated.

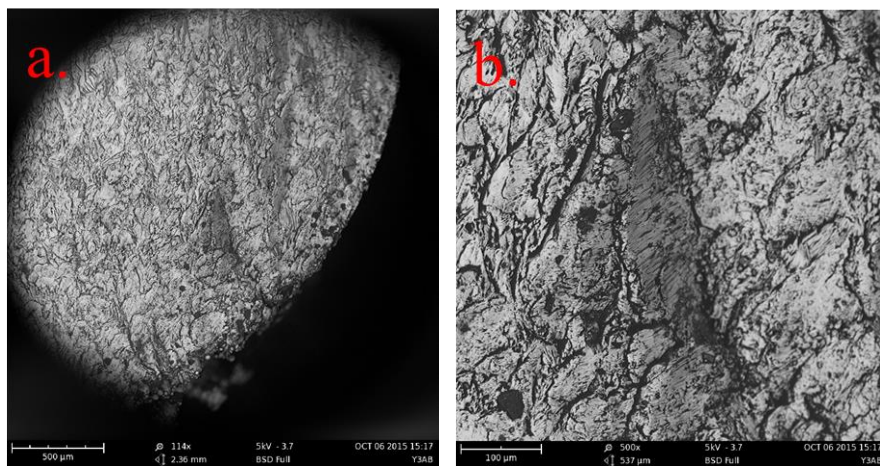


Figure 8-14. SEM Images of (a.) Crack Initiation [114X] and (b.) Crack Propagation Regions [500X] (As-Fabricated Y3 Specimen)

Striation marks are evident in the magnified image of Fig. 8-14(b.) indicating crack progression.

Overall, the fatigue specimen fracture surfaces include features consistent with ductile fatigue failures, such as fine striation marks in the crack propagation regions and microscopic dimples in the final fracture regions. The as-fabricated specimens clearly indicated the impact of the rough surface quality, with multiple crack initiation sites at different points around the specimen and a jagged surface indicating crack formation within different layers. The machined specimens, on

the other hand, exhibited a more classic fatigue fracture pattern, with smooth surfaces and easily recognizable initiation, propagation, and fracture regions.

9 CONCLUSIONS AND FUTURE WORK

9.1 SUMMARY OF RESULTS AND CONCLUSIONS

In order for AM to become a reliable manufacturing technology for functional, end-use parts, it will be necessary to characterize the resultant material properties and how these are impacted by process parameters and build orientation. The research in this thesis contributed to this effort by examining fatigue behavior of the nickel alloy Inconel 718 produced via DMLS in multiple build orientations with different surface finishes.

Surface roughness characterization completed herein showed average roughness values, Ra, between 4 and 8 μm for the as-fabricated specimens, with higher roughness found in the specimens built in a vertical orientation than those built horizontally. These average roughness values are consistent with published values in the literature for similar AM processes and materials.

Monotonic properties determined via tensile testing were found to be anisotropic with respect to build orientation. Average yield and ultimate tensile strength values were approximately 10% less in the Z orientation than in the X orientation, while the elastic modulus in the Z orientation was less than half that of the X orientation. Elongation values obtained showed slightly greater ductility in the Z orientation as well. The ultimate tensile and yield strength results obtained showed good agreement in each build orientation with published data. The large difference in modulus (over 50%) between orientations warrants further investigation in future efforts.

Both surface quality and build orientation were found to have a significant impact on material fatigue behavior. Fatigue lives were between 10 and nearly 1000 times greater in machined specimens versus as-fabricated specimens at equivalent stress levels, indicating the significant influence of the surface quality characteristic of the AM process. Additionally, results showed fatigue lives to be greater in the X/Y orientation than in the Z orientation for both machined and as-fabricated specimens. It was determined that, based on the trends in the S-N diagram developed, the endurance limit of the materials was approached at the lowest stress level tested, indicating that the endurance limit for the X/Y orientation was approximately 16% greater than that of the Z orientation. As-fabricated specimens also showed a clear anisotropy, with lives approximately 2.5-3 times greater at equivalent stress levels tested.

A comparison with published fatigue data for traditionally processed Inconel 718 showed good correlation with machined specimens in the horizontal (X/Y) build orientations. Furthermore, a comparison with empirical S-N curve relationships based on monotonic properties, although intended for steels, provided a close approximation to machined specimen results, verifying that this approach may be a useful tool for engineers to estimate material behavior during the design phase.

Finally, fractography was performed using a SEM. Porosity was evident in the tensile specimens, consistent with the literature, and likely influenced both tensile and fatigue behavior of the material. Fracture surfaces of machined fatigue specimens followed a classic pattern, with clear crack initiation, propagation, and final fracture regions. As-fabricated fatigue specimens were far more jagged and

showed evidence of multi-site crack initiation, consistent with the literature.

Ductile material behavior was evident, with striation marks and dimpled fracture regions.

Overall, results herein show that, with optimal surface quality and build orientation, fatigue behavior of DMLS-produced Inconel 718 approaches that of traditionally processed material. Combining these findings with a better understanding of the impact of other process parameters, it is likely that end-use parts can be built using DMLS that equal or even exceed the capabilities of traditionally processed material.

9.2 FUTURE EFFORTS

There is an abundance of future potential research efforts that can build upon the findings herein. As previously mentioned, additional tensile testing in different build orientations is recommended to further evaluate the differences found in elastic modulus. Also, fatigue testing of the as-fabricated specimens could be continued at lower stress levels in order to evaluate whether the data plateaus and to predict an endurance limit. Similarly, fatigue testing of a larger number of machined specimens near 70% of yield strength would refine the endurance limit prediction for the material. Determine residual stress levels and porosity levels in the material, as well as performing metallography to evaluate microstructure, would provide further insight into the material behavior as well.

This research could also be extended to Inconel 718 specimens with various post-build treatments, such as HIP, shot-peening, heat treatment, etc. in order to provide

valuable information on how these typical processes impact properties. Also, performing heat treatments similar to those typically applied to Inconel 718 would allow for a more direct comparison with published properties and data for the wrought material. An obvious extension of the work herein would involve comparing results for the same material across different AM processes. Furthermore, simply performing the same research on different materials would be beneficial as libraries of data are necessary, particularly for fatigue performance.

Another possible extension of this work relates to assessing the impact of AM process parameters on the material fatigue behavior. Beyond build orientation and surface quality, equipment process parameters such as laser scan strategy, laser scan speed, laser power, and even simply the location of the specimen on the build tray require assessment in relation to material behavior.

Finally, the primary focus of this effort was a stress-based approach to fatigue, where HCF behavior was characterized and S-N curves were developed. Additional research is needed on LCF behavior of these materials via strain-controlled testing. Fatigue behavior could also be assessed from a fracture mechanics perspective, evaluating crack propagation in additive manufactured materials and how this is impacted by build layers.

BIBLIOGRAPHY

- [1] Guo, Nannan and Ming C. Leu. "Additive Manufacturing: Technology, Applications and Research Needs." *Frontiers of Mechanical Engineering* 8.3 (2013): 215-243.
- [2] Gu, D.D., W. Meiners, K. Wissenbach, R. Poprawe. "Laser Additive Manufacturing of Metallic Components: Materials, Processes and Mechanisms." *International Materials Review* 57.3 (2012): 133-164.
- [3] "Fit to Print: New Plant Will Assemble the World's First Passenger Jet Engine with 3D Printed Fuel Nozzles, Next-Gen Materials." General Electric, 23 January 2014. <www.gereports.com/post/80701924024/fit-to-print>
- [4] "SpaceX Completes Qualification Testing of SuperDraco Thruster." Space Exploration Technologies Corporation, 27 May 2014. <www.spacex.com/press/2014/05/27/spacex-completes-qualification-testing-superdraco-thruster>
- [5] Brandl, Erhard, U. Heckenberger, V. Holzinger, D. Buchbinder. "Additive Manufactured AlSi10Mg Samples using Selective Laser Melting (SLM): Microstructure, High Cycle Fatigue, and Fracture Behavior." *Materials and Design* 34 (2012): 159-169.
- [6] Herderick, E. "Additive Manufacturing of Metals: A Review." *Proceedings of Materials Science & Technology 2011: Additive Manufacturing of Metals*. Columbus, OH, 2011.

- [7] Spierings, A. B., T. L. Starr, and K. Wegener. "Fatigue Performance of Additive Manufactured Metallic Parts." *Rapid Prototyping Journal* 19.2 (2013): 88-94.
- [8] Stephens, Ralph I., Ali Fatemi, Robert Stephens, Henry Fuchs. *Metal Fatigue in Engineering*. 2nd Edition. New York, NY: John Wiley and Sons, 2001.
- [9] Askeland, Donald and Pradeep Phule. *Essentials of Materials Science and Engineering*. Toronto, Ontario, Canada: Thomson, 2004.
- [10] ASTM E1823-13. "Standard Terminology Relating to Fatigue and Fracture Testing." West Conshohocken, PA: ASTM International, 2013.
- [11] Dowling, Norman E. *Mechanical Behavior of Materials: Engineering Methods for Deformation, Fracture, and Fatigue*. 4th Edition. Upper Saddle River, New Jersey: Pearson, 2013.
- [12] Juvinall, Robert C. and Kurt M. Marshek. *Fundamentals of Machine Component Design*. 4th Edition. Hoboken, NJ: John Wiley and Sons, 2006.
- [13] Bannantine, Julie, Jess Comer, and James Handrock. *Fundamentals of Metal Fatigue Analysis*. Englewood Cliffs, New Jersey: Prentice Hall, 1990.
- [14] Schutz, Walter. "A History of Fatigue." *Engineering Fracture Mechanics* 54.2 (1996): 263-300.
- [15] Lee, Yung-Li, et al. *Fatigue Testing and Analysis: Theory and Practice*. Burlington, MA: Elsevier Butterworth-Heinemann, 2005.

- [16] Instron Corporation. *Instron R.R. Moore High Speed Rotating Beam Fatigue Testing Machine - Operating Instructions Manual No. 000058-02-0604-EN*. Norwood, MA: Instron Corporation, 2004.
- [17] ASTM F2792-12a. "Standard Terminology for Additive Manufacturing Technologies." West Conshohocken, PA: ASTM International, 2012.
- [18] Bourell, David L., et al. "A Brief History of Additive Manufacturing and the 2009 Roadmap for Additive Manufacturing: Looking Back and Looking Ahead." *US-Turkey Workshop on Rapid Technologies*, September 24, 2009.
- [19] Shellabear, M. and O. Nyrhila. "DMLS – Development History and State of the Art." Presented at *Laser Assisted Net Shape Engineering (LANE) 2004 Conference*. Erlangen, Germany, Sept. 21-24, 2004.
- [20] Gibson, Ian, David Rosen, and Brent Stucker. *Additive Manufacturing Technologies: 3D Printing, Rapid Prototyping, and Direct Digital Manufacturing*. 2nd Edition. New York: Springer, 2015.
- [21] Horn, Timothy J. and Ola L. A. Harrysson. "Overview of Current Additive Manufacturing Technologies and Selected Applications." *Science Progress* 95.3 (2012): 255.
- [22] "Solid Print: Making Things with a 3D Printer Changes the Rules of Manufacturing." *The Economist*, 21 April 2012.
<<http://www.economist.com/node/21552892>>

- [23] General Electric Corporation. "Additive Manufacturing." 2015.
<<http://www.ge.com/stories/advanced-manufacturing>>
- [24] "3D Printing Market to Grow 23% Annually." *Metal Powder Report* 69.1 (2014): 42.
- [25] Vayre, B., F. Vignat, and F. Villeneuve. "Metallic Additive Manufacturing: State-of-the-Art Review and Prospects." *Mechanics and Industry* 13.2 (2012): 89-96.
- [26] Levy, G. N., R. Schindel, and J.-P. Kruth. "Rapid Manufacturing and Rapid Tooling with Layer Manufacturing (LM) Technologies, State of the Art and Future Perspectives." *CIRP Annals - Manufacturing Technology* 52.2 (2003): 589-609.
- [27] Kruth, J.-P., et al. "Consolidation Phenomena in Laser and Powder-Bed Based Layered Manufacturing." *CIRP Annals - Manufacturing Technology* 56.2 (2007): 730-59.
- [28] "EOS GmbH – Taking the Laser Lead." *Metal Powder Report* 69.3 (2014): 24-27.
- [29] Electro-Optical Systems GmbH. *EOS e-Manufacturing Solutions*.
<<http://www.eos.info/en>>.

[30] Scott-Emuakpor, O., et al. "Bending Fatigue Life Characterization of Direct Metal Laser Sintering Nickel Alloy 718." *Fatigue and Fracture of Engineering Materials and Structures* 00 (2015): 1-13.

[31] Amsterdam, E., and G. A. Kool. "High Cycle Fatigue of Laser Beam Deposited Ti-6Al-4V and Inconel 718." *ICAF 2009, Bridging the Gap Between Theory and Operational Practice - Proceedings of the 25th Symposium of the International Committee on Aeronautical Fatigue* (2009): 1261 – 1274.

[32] Kirka, M., et al. "Mechanical and Microstructure Attributes of Inconel 718 Processed Via Electron Beam Melting." *Proceedings – American Society for Precision Engineering (ASPE) 2015 Spring Topical Meeting: Achieving Precision Tolerances in Additive Manufacturing*. North Carolina State University, Raleigh, NC, April 2015.

[33] Wang, Fude, et al. "Microstructure and Mechanical Properties of Wire and Arc Additive Manufactured Ti-6Al-4V." *Metallurgical and Materials Transactions A* 44A (2013): 968–977.

[34] Bian, Linkan, Scott M. Thompson, and Nima Shamsaei. "Mechanical Properties and Microstructural Features of Direct Laser-Deposited Ti-6Al-4V." *JOM* 67.3 (2015): 629-38.

[35] Svensson, M. "Ti6Al4V Manufactured with Electron Beam Melting (EBM): Mechanical and Chemical Properties." *Presented at Aeromat 2009*. Dayton OH, June 2009.

- [36] Frazier, William E. "Metal Additive Manufacturing: A Review." *Journal of Materials Engineering and Performance* 23.6 (2014): 1917-1928.
- [37] Leuders, S., et al. "On the Mechanical Behaviour of Titanium Alloy TiAl6V4 Manufactured by Selective Laser Melting: Fatigue Resistance and Crack Growth Performance." *International Journal of Fatigue* 48 (2013): 300-307.
- [38] Edwards, P. and M. Ramulu. "Fatigue Performance Evaluation of Selective Laser Melted Ti-6Al-4V." *Materials Science and Engineering A* 598 (2014): 327-337.
- [39] Edwards, P., A. O'Conner, and M. Ramulu. "Electron Beam Additive Manufacturing of Titanium Components: Properties and Performance." *Journal of Manufacturing Science and Engineering* 135.6 (2013).
- [40] Chan, K. S., M. Koike, R. L. Mason, and T. Okabe. "Fatigue Life of Titanium Alloys Fabricated by Additive Layer Manufacturing Techniques for Dental Implants." *Metallurgical and Materials Transactions A* 44A (2013): 1010-1022.
- [41] Rafi, H. Khalid, T. L. Starr, and B. E. Stucker. "A Comparison of the Tensile, Fatigue, and Fracture Behavior of Ti-6Al-4V and 15-5 PH Stainless Steel Parts made by Selective Laser Melting." *International Journal of Advanced Manufacturing Technology* 69 (2013): 1299-1309.
- [42] Wycisk, E., et al. "Effects of Defects in Laser Additive Manufactured Ti-6Al-4V on Fatigue Properties," *Physics Procedia* 56 (2014): 371-378.

- [43] Baufeld, Bernd. "Mechanical Properties of Inconel 718 Parts Manufactured by Shaped Metal Deposition (SMD)." *Journal of Materials Engineering and Performance* 21.7 (2012): 1416-21.
- [44] Larosa, Maria Aparecida, et al. "Microstructural and Mechanical Characterization of a Custom-Built Implant Manufactured in Titanium Alloy by Direct Metal Laser Sintering." *Advances in Mechanical Engineering* 2014 (2014).
- [45] Manfredi, Diego, et al. "From Powders to Dense Metal Parts: Characterization of a Commercial AlSiMg Alloy Processed through Direct Metal Laser Sintering." *Materials* 6.3 (2013): 856-69.
- [46] Becker, T. H., M. Beck, and C. Scheffer. "Microstructure and Mechanical Properties of Direct Metal Laser Sintered Ti-6Al-4V." *South African Journal of Industrial Engineering* 26.1 (2015): 1-10.
- [47] Leuders, Stefan, et al. "Fatigue Strength Prediction for Titanium Alloy TiAl6V4 Manufactured by Selective Laser Melting." *Metallurgical and Materials Transactions* 46.9 (2015): 3816-23.
- [48] Sanz, C. and V. García Navas. "Structural Integrity of Direct Metal Laser Sintered Parts Subjected to Thermal and Finishing Treatments." *Journal of Materials Processing Technology* 213.12 (2013): 2126-2136.
- [49] Kruth, J.-P, et al. "Part and Material Properties in Selective Laser Melting of Metals." *16th International Symposium on Electromachining, ISEM* (2010).

- [50] ASTM F3055-14. “Standard Specification for Additive Manufacturing Nickel Alloy (UNS N07718) with Powder Bed Fusion.” West Conshohocken, PA: ASTM International, 2014.
- [51] ASTM E8/E8M-13a. “Standard Test Methods for Tension Testing of Metallic Materials.” West Conshohocken, PA: ASTM International, 2013.
- [52] ASTM E466-07. “Standard Practice for Conducting Force Controlled Constant Amplitude Axial Fatigue Tests of Metallic Materials.” West Conshohocken, PA: ASTM International, 2007.
- [53] ASTM E739-10. “Standard Practice for Statistical Analysis of Linear or Linearized Stress-Life (S-N) and Strain-Life (ϵ -N) Fatigue Data.” West Conshohocken, PA: ASTM International, 2010.
- [54] Zygo Corporation. *NewView 600 Operating Manual OMP-0528B*. Middlefield, CT: Zygo Corporation, 2007.
- [55] Oberg, E., F. Jones, H. Horton, and H. Ryffel. *Machinery’s Handbook, 29th Edition*. New York, NY: Industrial Press, 2012.
- [56] “EOS Nickel Alloy IN718 Data Sheet.” EOS GmbH – Electro Optical Systems, 2014. <www.eos.info/material-m>
- [57] Battelle Memorial Institute. *Metallic Materials Properties Development and Standardization (MMPDS-09)*. Columbus, OH: Battelle Memorial Institute, 2014.

APPENDIX A

A1 AS-FABRICATED X ORIENTATION DATA

Table A-1. As-Fabricated X Orientation Specimen Dimensions

Specimen No.	Length (in)	Diameter 1 (in)	Diameter 2 (in)	Center Diameter (in)	Runout (in)
1	3.528	0.368	0.3715	.200 min/.210 max	0.015
2	3.496	0.37	0.3735	.198 min/.215 max	0.026
3	3.492	0.371	0.374	.198 min / .211 max	0.037

Table A-2. As-Fabricated X Orientation Specimen Fatigue Test Data

Specimen No.	Applied Load (lbs)	Percentage of Yield Strength	RPM	Frequency (Hz)	Cycles to Failure
1	16	70%	6300	105.0	68026
2	19	80%	6200	103.3	52562
3	23	90%	6100	101.7	38279

Notes:

- Maximum/minimum center diameters are a result of the surface roughness on the X and Y orientation as-built specimens. Measuring the diameter from the smooth “top” side of the specimen to the rough “bottom” side results in a larger diameter than measuring the diameter 90 degrees away. Both measurements are recorded here.

A2 AS-FABRICATED Y ORIENTATION DATA

Table A-3. As-Fabricated Y Orientation Specimen Dimensions

Specimen No.	Length (in)	Diameter 1 (in)	Diameter 2 (in)	Center Diameter (in)	Runout (in)
1	3.525	0.368	0.371	.199 min/.212 max	0.016
2	3.497	0.3685	0.3715	.199 min/.211 max	0.023
3	3.495	0.3695	0.373	.199 min/.212 max	0.031

Table A-4. As-Fabricated Y Orientation Specimen Fatigue Test Data

Specimen No.	Applied Load (lbs)	Percentage of Yield Strength	RPM	Frequency (Hz)	Cycles to Failure
1	16	70%	6200	103.3	84422
2	19	80%	6200	103.3	49900
3	23	90%	6000	100.0	35753

Notes:

- Maximum/minimum center diameters are a result of the surface roughness on the X and Y orientation as-built specimens. Measuring the diameter from the smooth “top” side of the specimen to the rough “bottom” side results in a larger diameter than measuring the diameter 90 degrees away. Both measurements are recorded here.

A3 AS-FABRICATED Z ORIENTATION DATA

Table A-5. As-Fabricated Z Orientation Specimen Dimensions

Specimen No.	Length (in)	Diameter 1 (in)	Diameter 2 (in)	Center Diameter (in)	Runout (in)
1	3.428	0.368	0.371	0.198	N/A
2	3.4275	0.368	0.372	0.199	N/A
3	3.428	.368-.370	.372 - .375	0.198	N/A
4	3.437	.370-.372	.368-.369	0.198	N/A
5	3.4295	.368-.370	.372-.375	0.198	N/A
6	3.437	.367-.370	.369-.371	0.198	N/A
7	3.436	.370-.372	0.368	0.198	N/A
8	3.428	.371-.372	.368-.369	0.198	N/A
9	3.432	.371-.373	0.368	0.198	N/A

Table A-6. As-Fabricated Z Orientation Specimen Fatigue Test Data

Specimen No.	Applied Load (lbs)	Percentage of Yield Strength	RPM	Frequency (Hz)	Cycles to Failure
1	19	90%	6000	100.0	20442
2	16	80%	5400	90.0	23172
3	12.5	70%	5500	91.7	48188
4	19	90%	5500	91.7	19786
5	16	80%	6000	100.0	27424
6	12.5	70%	5600	93.3	52388
7	12.5	70%	6000	100.0	40869
8	19	90%	5900	98.3	19566
9	16	80%	6100	101.7	26569

A4 MACHINED X ORIENTATION DATA

Table A-7. Machined X Orientation Specimen Dimensions

Specimen No.	Length (in)	Diameter 1 (in)	Diameter 2 (in)	Center Diameter (in)	Runout (in)
2	3.440	0.3710	0.372	0.201	N/A
3	3.446	0.3710	0.370	0.202	N/A
4	3.455	0.3715	0.369	0.203	0.022
5	3.463	0.3720	0.369	0.203	0.025
6	3.469	0.3715	0.369	0.203	0.018
7	3.400	0.3750	0.372	0.206	0.022
8	3.463	0.3750	0.372	0.206	0.037

Table A-8. Machined X Orientation Specimen Fatigue Test Data

Specimen No.	Applied Load (lbs)	Percentage of Yield Strength	RPM	Frequency (Hz)	Cycles to Failure
2	23	90%	6100	101.7	283499
3	23	90%	6000	100.0	324348
4	19	80%	6200	103.3	305323
5	16	70%	6000	100.0	113073797*
6	16	70%	6300	105.0	619152
7	16	70%	5700	95.0	2172122
8	19	80%	5800	96.7	427676

Notes:

- Specimen No. 5 did not break and was stopped at the number of cycles indicated (marked with an asterisk).
- The equipment stopped and required motor bushing cleaning in the middle of testing on specimen No.'s 4, 5, and 7. Testing was restarted after cleaning on each and completed without issue. The counter stored the number of cycles at when the equipment stopped, thus after restart the new cycles were simply added to this total resulting in the cumulative number of cycles.

A5 MACHINED Y ORIENTATION DATA

Table A-9. Machined Y Orientation Specimen Dimensions

Specimen No.	Length (in)	Diameter 1 (in)	Diameter 2 (in)	Center Diameter (in)	Runout (in)
1	3.439	0.3710	0.371	0.197	N/A
2	3.438	0.3670	0.367	0.198	N/A
3	3.436	0.3705	0.371	0.206	N/A
4	3.465	.368-.369	0.366	0.200	0.042
5	3.472	0.3740	0.371	0.205	0.045
6	3.488	0.3735	0.371	0.205	0.034
7	3.466	0.3700	0.367	0.201	0.030
8	3.482	0.3745	0.372	0.206	0.032

Table A-10. Machined Y Orientation Specimen Fatigue Test Data

Specimen No.	Applied Load (lbs)	Percentage of Yield Strength	RPM	Frequency (Hz)	Cycles to Failure
1	23	90%	5700	95.0	176669
2	23	90%	5900	98.3	314845
3	23	90%	6000	100.0	81482
4	19	80%	5800	96.7	375229
5	19	80%	6400	106.7	171034
6	16	70%	6200	103.3	5204336
7	16	70%	6300	105.0	460860
8	16	70%	6200	103.3	56093297

Notes:

- The equipment stopped and required motor bushing cleaning in the middle of testing on specimen No.'s 4 and 6. Testing was restarted after cleaning on each and completed without issue. The counter stored the number of cycles at when the equipment stopped, thus after restart the new cycles were simply added to this total resulting in the cumulative number of cycles.

A6 MACHINED Z ORIENTATION DATA

Table A-11. Machined Z Orientation Specimen Dimensions

Specimen No.	Length (in)	Diameter 1 (in)	Diameter 2 (in)	Center Diameter (in)	Runout (in)
1	3.442	0.3710	0.371	0.202	N/A
3	3.445	0.3710	0.370	0.199	N/A
4	3.498	0.3720	0.370	0.204	0.010
5	3.470	0.3720	0.370	0.204	0.009
6	3.465	0.3730	0.370	0.204	0.007
7	3.46750	0.3695	0.37300	0.20400	0.010
8	3.462	0.3690	0.372	0.204	0.010
9	3.453	0.3700	0.373	0.204	0.006

Table A-12. Machined Z Orientation Specimen Fatigue Test Data

Specimen No.	Applied Load (lbs)	Percentage of Yield Strength	RPM	Frequency (Hz)	Cycles to Failure
1	19	90%	5700	95.0	204563
3	19	90%	5700	95.0	146258
4	16	80%	5800	96.7	851990
5	16	80%	6100	101.7	333815
6	12.5	70%	6000	100.0	27715045
7	19	90%	6300	105.0	382475
8	16	80%	6300	105.0	383383
9	12.5	70%	6300	105.0	47659676

Notes:

- The equipment stopped and required motor bushing cleaning in the middle of testing on specimen No. 9. Testing was restarted after cleaning on each and completed without issue. The counter stored the number of cycles at when the equipment stopped, thus after restart the new cycles were simply added to this total resulting in the cumulative number of cycles.
- Specimens No.'s 6 and 7 slipped out of the bushings in the middle of testing. Both were reinserted and tightened, and completed without issue.